



This is to certify that the

dissertation entitled Optimization of Metal-Ceramic Bonding to Enhance Mechanical Properties of Ceramic Matrix Composite

presented by

Taekoo Lee

has been accepted towards fulfillment of the requirements for

Ph.D. degree in Materials Science

Major professor

Date 9-29-93

MSU is an Affirmative Action/Equal Opportunity Institution

0-12771

LIBRARY Michigan State University

PLACE IN RETURN BOX to remove this checkout from your record.

TO AVOID FINES return on or before date due.

DATE DUE	DATE DUE	DATE DUE

MSU is An Affirmative Action/Equal Opportunity Institution

Optimization of Metal-Ceramic Bonding to Enhance Mechanical Properties of Ceramic Matrix Composite

by

Taekoo Lee

A DISSERTATION

submitted to

Michigan State University
in partial fulfillment of the requirements
for the degree of

DOCTOR OF PHILOSOPHY

Department of Materials Science and Mechanics
1993

K. N. Subramanian, Advisor

Abstract

Optimization of Metal-Ceramic Bonding to Enhance Mechanical
Properties of Ceramic Matrix Composite

by

Taekoo Lee

The role of interface on the fracture toughness of ceramic glass reinforced with metallic ribbon was investigated. A strong interfacial bonding strength is essential for the load transfer between the matrix and ribbon, and for the utilization of the ductility of the reinforcement. However, weak interfacial bonding is considered to be important so that ribbon pull-out can improve the toughness of brittle ceramic matrix composites. The main aim of the present study is to carry out interface design to optimize mechanical properties of brittle ceramic matrix composites reinforced with ductile metallic ribbons.

Acknowledgment

The author wishes to express his sincere gratitude to his major thesis advisor Dr. K.N. Subramanian for his generous assistance and guidance which ultimately led to the completion of the work reported in this dissertation.

The author is also grateful to the members of his doctoral committee, Dr. David S. Grummon, Dr. Dashin Liu and Dr. Carl Foiles, who with their helpful and understanding attitude greatly encouraged him in the course of his research.

Thanks are also extended to the Composite Materials and Structures Center at Michigan State University for financial support during the doctoral program.

Finally, and above all, I wish to express my deepest thanks to my parents, my lovely wife, Suekyung, and son, Kwangmin, for their consistent support, encouragement and understanding, throughout the course of this study.

Contents

LIST OF TABLES		7
LIST OF FIGURES		V
1. Introduction		1
2. Literature Survey		
2-1. Evaluation of Inte	rfacial Bonding Strength in Ceramic	
Matrix Composite		
2-1-1. Interface Te	st Methods	6
2-1-2. Theoretical	Analyses of Interfacial Debonding and	
Fiber Pull-o	ut during Interface Tests 1	1
2-2. Fracture Toughne	ss Measurements in Ceramic Matrix	
Composites		7
2-3. Strength Analyses	s in Ceramic Matrix Composites 2	21
3. Experimental Proceed	lure	
3-1. Materials	2	24
3-2. Composite Fabrica	ation 2	25
3-3. Interface Modifica	tion	
3-3-1. Thermal Cy	cling Technique2	29
3-3-2. Acid Etchin	g Technique 3	2
3-4. Mechanical Testir	ng 3	2
3-5. Micrographic Obse	ervation 3	6
4. Results and Discussi	on	
4-1. Theoretical and E	xperimental Analysis of Debonding Pro-	
cess of Ductile Rib	bon Embedded in Brittle Matrix	
4-1-1. Theoretical	Modelling 3	7

4-1-1. Load Required to Initiate Debonding	38
4-1-1-2. Load Required for Continuation of Debond-	
ing	40
4-1-2. Experimental Analysis	44
4-2. Interface Modifications	
4-2-1. Thermal Cycling Technique	56
4-2-1-1. Effects of Thermal Cycling on The Interfa-	
cial Bonding Strength and Frictional Shear	
Stress	64
4-2-1-2. Effects of Thermal Cycling on The Com-	
plete Debonding Stress	67
4-2-2. Acid Etching of The Ribbon	73
4-3. Fracture Toughness Behavior	
4-3-1. Effect of Fracture Toughness (K_{1c}) on Interfacial	
Bonding	87
4-3-2. Tensile Behavior of Pre-cracked Composite	92
4-3-3. Toughness due to Crack Bridging(ΔG_c)	94
5. Conclusions	100
6. References	103

List of Tables

Table 1.	Physical and mechanical properties of constituents of	
	the composite.	27
Table 2.	Measured interfacial properties of 650-TC specimens	
	after various numbers of thermal cycles.	62
Table 3.	Measured interfacial properties of thermal cycled speci-	
	mens up to various maximum temperatures after 5 ther-	
	mal cycles.	63
Table 4.	Fracture toughness (K_{1c}) of soda-lime glass matrix rein-	
	forced Nichrome ribbon with various bonding conditions.	88
Table 5.	Effect of interfacial bonding on the displacement at the	
	ribbon fracture.	93
Table 6.	Fracture toughness due to crack bridging (ΔG_c) in vari-	
	ous bonding conditions.	95
Table 7.	Critical embedded length (l_e) for the maximum fracture	
	toughness due to crack bridging in various bonding con-	
	ditions.	98

List of Figures

Fig. 1	A schematic illustrating mechanisms of toughening in	
	ceramic matrix reinforced with ceramic fibers	
Fig. 2	A schematic illustrating mechanisms of toughening in	
	ceramic matrix reinforced with metallic fibers	
Fig. 3	Schematic diagrams of indentation techniques:	
	(a) with microhardness indenter(thick specimen),	
	(b) with spherical indenter(thick specimen)	
	(c) push-through specimen (thin slice of the composite).	
Fig. 4	Schematic diagram of the fiber push-through and push-	
	back apparatus.	
Fig. 5	(a) Variation in average interfacial shear stress with	
	embedded fiber length.	
	(b) Variation in maximum pull-out load with embedded	
	fiber length.	
Fig. 6	Variation of maximum pull-out load:	
	(a) as a function of embedded fiber length,	
	(b) as a function of fiber displacement, for various friction	
	conditions.	
Fig. 7	Dugdale-Barenblatt crack model:	
	(a) Cohesive zone at crack tip with restraining stress	
	dependent on separation distance	
	(b) Force-displacement relation for atomic attraction in	
	elastic brittle fracture.	
Ria 2	Tunical stress-strain curve of the Nichrome ribbon	

	obtained from tensile test.
Fig. 9	The schematics of sandwiching of a series of aligned rib-
	bons between the glass slides:
	a) general set-up
	b) composite from which pull-out test samples were cut
	out
	c) composite from which fracture toughness test samples
	were cut out
Fig. 10	The schematic of typical pull-out specimen.
Fig. 11	The schematics of typical fracture toughness test speci-
	mens:
	a) single notched specimen for flexure test
	b) pre-cracked specimens for tensile test.
Fig. 12	Schematics of experimental details of the tensile test:
	a) general set-up
	b) self-aligning fixture.
Fig. 13	Shear stresses due to tensile loading at edge of the
	embedded area.
Fig. 14	Load (P) required for continuation of debonding
Fig. 15	Static frictional force at the debonded interface
Fig. 16	Typical load-displacement curve obtained in pull-out
	tests of Nichrome ribbon embedded in soda lime glass
	matrix.
Fig. 17	SEM micrograph of the partially debonded interface
	between the Nichrome ribbon and the soda lime glass
	matrix.
Fig. 18	Mechanical keying of debonded surfaces produced by

	roughness of debonded surfaces, transverse contraction,
	and longitudinal plastic extension of the ribbon due to
	tensile loading after debonding.
Fig. 19	SEM micrograph of the interface between the Nichrome
	ribbon and soda lime glass matrix after debonding
	progresses to some degree.
Fig. 20	Interfacial shear stresses for debonding various embed-
	ded lengths of the Nichrome ribbon.
Fig. 21	Loads required to continue debonding as a function of
	debonded length.
Fig. 22	Effect of embedded length on the normal stress on the
	ribbon when debonding starts (σ_i), and normal stress
	when debonding is completed (σ_f) in soda lime slide glass
	reinforced with Nichrome ribbon
Fig. 23	Typical stress-displacement curves of as-fabricated, and
	650-TC specimens after various numbers of thermal
	cycles
Fig. 24	SEM micrographs at interfaces of:
	(a) as-fabricated specimens,
	(b) 650-TC specimen after 3 thermal cycles,
	(c) 650-TC specimen after 5 thermal cycles
Fig. 25	Stress-displacement curves of specimens that have
	undergone 5 thermal cycles with various maximum tem-
	peratures
Fig. 26	Interfacial bonding strengths of 650-TC specimens after
	various numbers of thermal cycles
Fig 97	The effect of maximum cyclic temperature on the interfa-

·-
·-
•
••••
.ce-
-
er.
es
or
8,
or
•••

treatment, composite fabrication, and during pull-out

	test for the composite with:	
	a) as-received ribbon roughened by etching,	83
	b) pre-oxidized ribbon roughened by etching.	84
Fig. 36	Pull-out stress of ribbons that have undergone various	
	treatments for an embedded length of 1.7 mm.	86
Fig. 37	Fractographic observation of the crack shielding by the	
	ribbon. Interference fringes represent the path of the	
	crack	90
Fig. 38	Typical stress-displacement curves obtained from the	
	tensile loading of the pre-cracked composite specimens	
	with various interfacial bonding conditions.	91
Fig. 39	Stress-displacement curves showing the effect of the	
	embedded ribbon length on toughness (ΔG_c) of NT com-	
	posite specimens.	97

1. Introduction

Ceramics are a promising class of structural materials for applications where high strength, high stiffness, low thermal expansion, low density and high temperature stability are desirable attributes. However, the brittleness of ceramics which catastrophically fail is always a problem in use of conventional ceramics as a structural materials. Ceramic matrix composites may achieve the marked improvements in mechanical properties, especially in fracture toughness, by reinforcements. The main goal of ceramic matrix composites is to reduce the brittleness of ceramics while retaining most of the strength of the ceramic matrix, for structural applications.

Various studies on fracture toughness and interfacial bonding in ceramic matrix reinforced with ceramic fibers have shown that high fracture toughness can be obtained in ceramic matrix composites that possess weak interfacial bonding (1-15). A major mechanism of enhancement of fracture toughness in such a composite system is the bridging of crack surfaces by intact fibers (Fig. 1). This involves the frictional sliding of fibers against the matrix following interfacial debonding and failure of the fibers. It requires weak interfacial bonding between the reinforcements and matrix. On the other hand, ceramic matrix composites containing metallic reinforcements strongly bonded to the matrix have exhibited profoundly high fracture toughness. The work done during plastic deformation of the metallic reinforcements between the crack surfaces in the bridging zone contributes to the overall toughness of these composites (16-28) (Fig. 2). Therefore, if both plastic deformation of the reinforcement and frictional sliding between the components can be utilized in the same composite, the

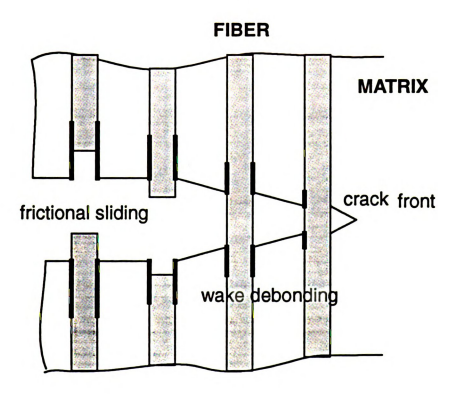


Fig. 1 A schematic illustrating mechanisms of toughening in ceramic matrix reinforced with ceramic fibers.

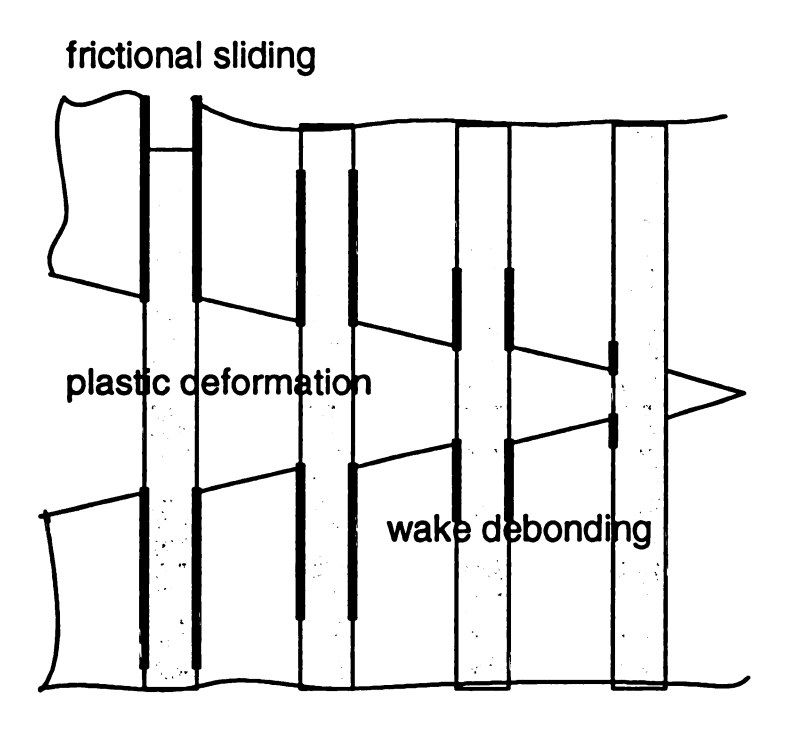


Fig. 2 A schematic illustrating mechanisms of toughening in ceramic matrix reinforced with metallic fibers.

fracture toughness of the ceramic matrix composite with metallic reinforcement may be significantly improved. Since such contributions are controlled by the interfacial bonding strength between the matrix and the reinforcement, the maximum fracture toughness can be achieved by modification of interfacial characteristics.

Several investigations of interfacial shear stress on fiber pull-out in ceramic matrix composites have been reported (29-36). However, the plastic behavior of the metallic fibers in brittle ceramic matrix composites has not been taken into account in analyses of fiber pull-out reported in literature. Slip due to plastic deformation of the metallic fiber may affect the distribution of shear stress at the bonded interfacial area. Moreover, the radial plastic contraction of the metallic fiber at tensile stresses beyond yield stress may take its surface out of contact with the matrix resulting in significantly reduced residual gripping pressure.

Coating of the reinforcements is the most widely used technique to modify the interfacial characteristics in ceramic matrix composites (37-40). Modification of the interface between the reinforcement and matrix by means of thermal cycling is also a possibility when the thermal expansion mismatch between the components is relatively large. Radial and tangential stresses are generated at the interface of the composite during cooling after composite fabrication due to the mismatch of thermal expansion coefficients between the reinforcement and matrix. These residual thermal stresses may cause microcracking at the interface or in the matrix, depending on the interfacial bonding strength and matrix strength of the composite. In glass matrix composites, microcracks present in the matrix can heal by viscous flow during heating portion of thermal cycling (41). However, microcracks in the interface layer can not be expected to self-heal. Instead,

with continued thermal cycling, such interfacial microcracks will link together, resulting in weaker interfacial bonding.

Interface modification can also be achieved by surface treatments such as chemical etching of the metallic reinforcements in as-received or pre-oxidized condition prior to the composite fabrication. Moore and Kunz (42) showed that in glass matrix composites containing metal particles, acid etching of pre-oxidized metal particles generates extensive, uniform surface roughness and that the cracks proceed along the roughened contour of the particles during the composite fracture. As a result, fracture toughness in this composite considerably improved with such a surface treatment of metal particles.

The principal aim of present study is to elucidate interfacial effects on mechanical properties of brittle matrix with ductile reinforcement, and finally to control the interfacial bonding strength in order to obtain optimum mechanical properties in the composite. Ribbon geometry of the reinforcement was selected in this study to facilitate ease of fabrication and theoretical modelling of the composite. First of all, a method to evaluate the interfacial bonding strength of this composite, single ribbon pull-out test was adopted in the present study to investigate the interfacial effects in this composite. Secondly, the interfacial characteristics between the ribbon and matrix were modified to obtain the optimum interfacial bonding in this composite by means of thermal cycling and acid etching techniques. Finally using the specimens with various interfacial bonding conditions achieved, increment in fracture toughness of the composite due to crack bridging was evaluated and consequently, optimum interfacial bonding strength for maximum fracture toughness in this composite was determined.

2. Literature Survey

2-1. Evaluation of Interfacial bonding strength in Ceramic Matrix Composite

2-1-1. Interface Test Methods

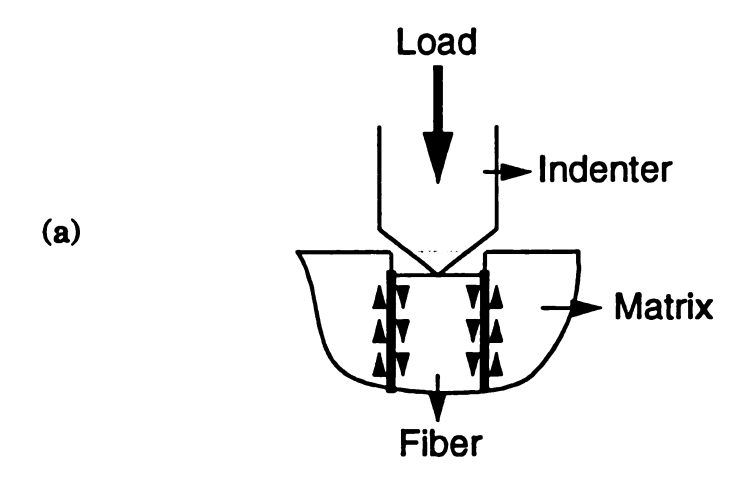
Due to importance of the interfacial properties in composites, numerous studies have focussed on controlling interfacial bonding strength by means of modifying interfacial characteristics to achieve desirable composite properties. Therefore, there is considerable interest in developing simple experimental techniques and adequate model for assessing interfacial properties. It may be possible to observe debonding initiation in transverse tension and calculate the bonding strength from micromechanics in some metal matrix composites (43). However, for most composites, this technique is not adequate because composite fracture precedes interfacial debonding (44).

The single fiber pull-out test has been widely used to assess interfacial properties of composites (29-36, 45-53). The pull-out test can determine the interfacial bonding strength from not only the stress conditions when debonding initiates, but also the frictional sliding resistance as the debonded fiber is pulled out from the matrix. However, this technique has difficulty in fabrication of the pull-out test specimens in ceramic matrix composites, and also the interface in specially prepared pull-out specimens may not be representative of the actual composites.

To avoid the difficulties associated with the pull-out tests in ceramic

matrix composite, Marshall has used microindentation method [Fig. 3(a)], which is referred to as push-out (or push-down) tests (54,55), to measure interfacial properties of glass ceramic composites reinforced with SiC fibers. This technique involves application of a force to the end of a fiber embedded in a matrix using a microhardness indenter. Interfacial shear stresses can be evaluated from the applied load and the displacement of the fiber. Grande et al. (44) have used a spherical indenter [Fig. 3(b)] instead of conventional Vickers microhardness indenter in order to get rid of the problem arising from sharp indenter; at high load, cracks may be introduced into the fibers that can influence the measurements. Since such indentation techniques use real composites, the problems involved in single fiber pull-out tests do not arise in these techniques. However, the identification of the debonding event involves a somewhat inaccurate procedure. Laughner et al. (56) have used thin slices of the composite specimens instead of thick specimens as a variation of the above techniques, which is sometimes referred to as a push-through method [Fig. 3(c)]. The thin slice is advantageous for frictional measurements for known debonded length; however, sufficiently thin slices are difficult to prepare properly and test, for small-diameter fiber systems. Recently an improved fiber push-through test has been designed by Warren et al. (57) in metal and glass matrix composites reinforced with SiC fibers (Fig. 4). This technique involves push-back procedure following push-through test, which can give additional information about frictional sliding characteristics of interface in such composites.

Since indentation techniques are not suitable for this study due to the geometry of the ribbon reinforcement, the single ribbon pull-out test was used in this study to evaluate interfacial behavior.



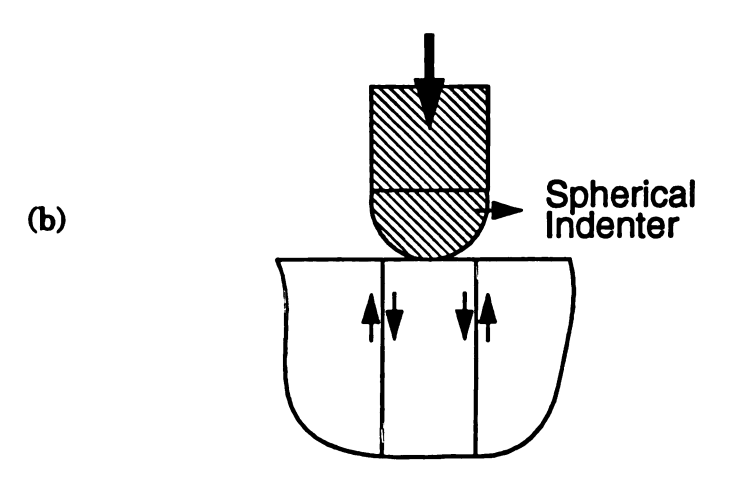


Fig. 3 Schematic diagrams of indentation techniques (a) with microhardness indenter (thick specimen), (b) with spherical indenter (thick specimen), and (c) push-through specimen (thin slice of the composite).

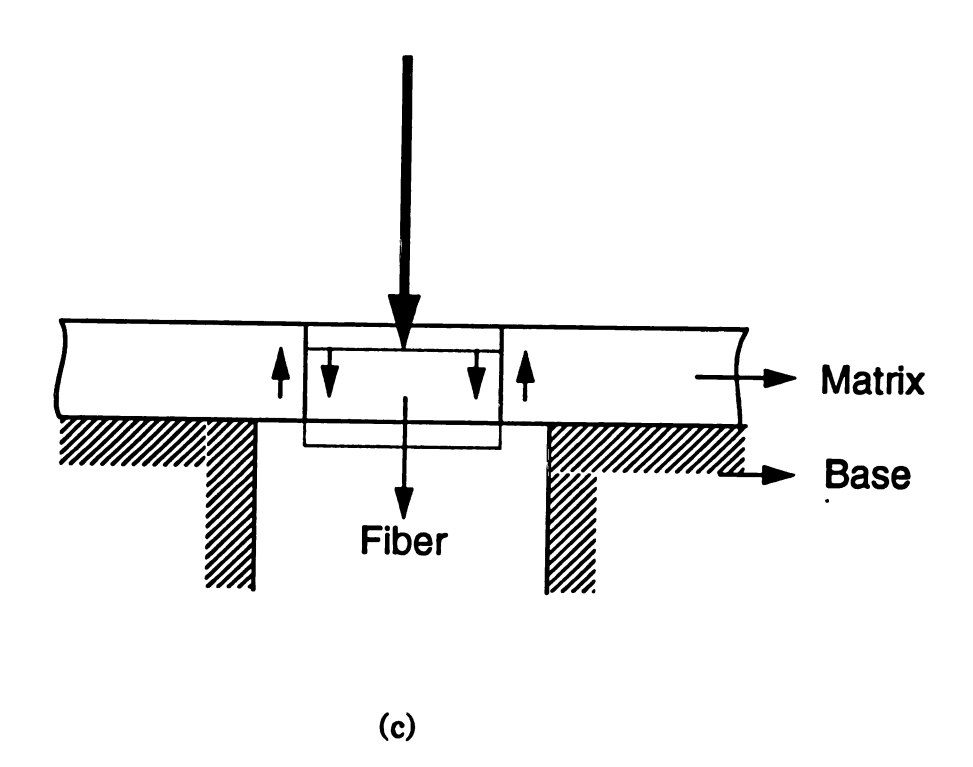


Fig. 3 (continued)

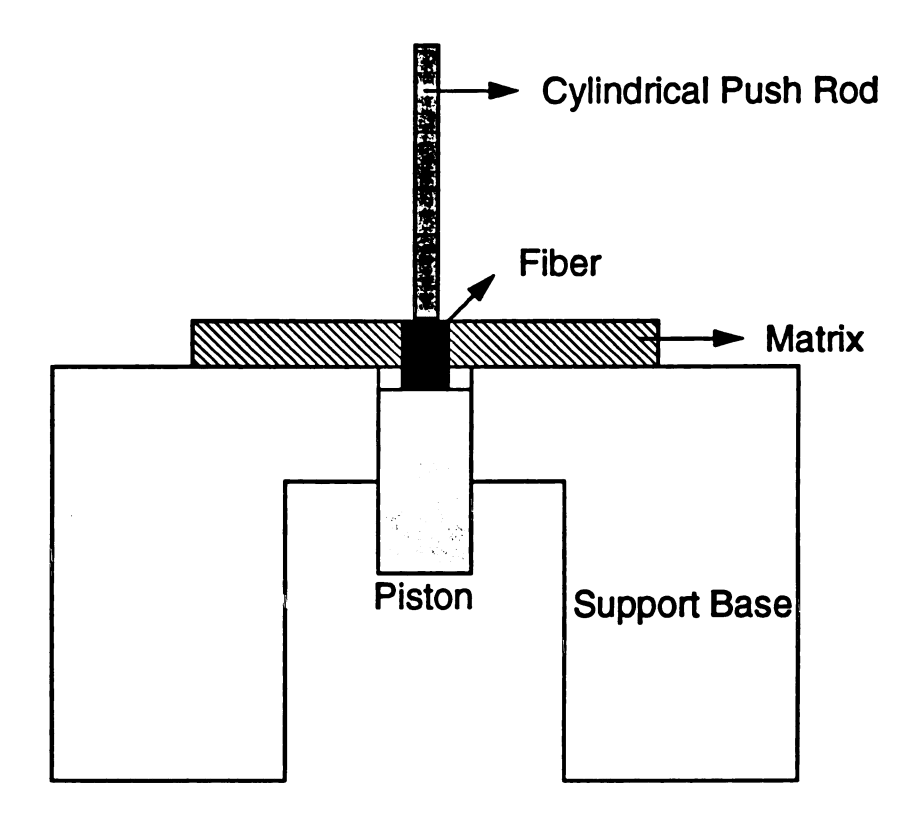


Fig. 4 Schematic diagram of the fiber push-through and push-back apparatus.

2-1-2. Theoretical Analyses of Interfacial Debonding and Fiber Pull-out during Interface Tests

A number of investigations of interfacial shear stress on fiber pull-out in composites have reported so as to evaluate the bonding strength between fiber and matrix, using above interface test methods (29-36). Kelly and Tyson (45) have assumed that shear stress at the interface is distributed uniformly along the fiber embedded into metal matrix. The stress in the fiber required to pull-out the fiber from metal matrix is given by

$$\sigma_f = 2\tau_s \frac{x}{r} \tag{Eq. 1}$$

where τ_s is the shear stress at the fiber/matrix interface, x is a distance from the end of the fiber, and r is the radius of the fiber. Since this assumption is based on the idea of metal-matrix yielding under high shear stress, it can not be applied to ceramic matrix composite in which the shear stresses at the interface are not alleviated by matrix yielding.

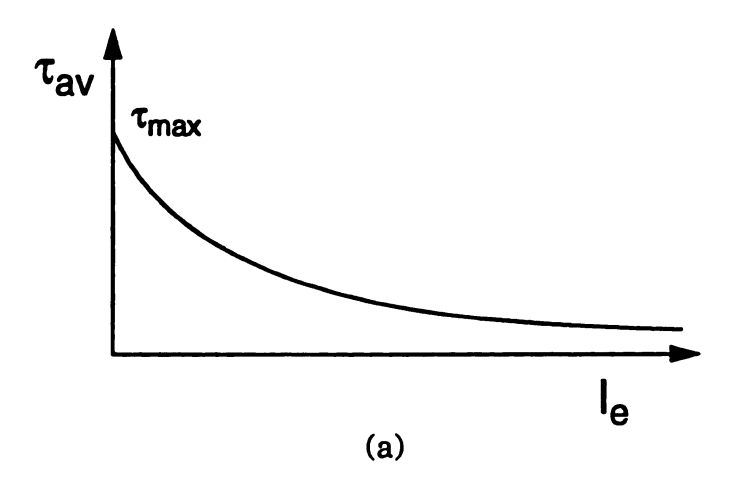
A general relationship between fiber/matrix interfacial shear stress and embedded fiber length in a pull-out specimen has been developed by Greszczuk (29), using the assumptions of shear-lag theory (58). The equilibrium of forces acting on an element of the fiber in a model pull-out specimen and the corresponding boundary conditions are considered. As a result, he has derived the maximum shear stress along the interface occurring at the point where the fiber enters the matrix, which is given by

$$\frac{\tau_{max}}{\tau_{av}} = \alpha l_e \coth \alpha l_e \tag{Eq. 2}$$

where τ_{av} is the average shear stress along the interface, l_e is embedded length of the fiber, and α is a shear-lag parameter dependent on elastic properties of the constituents and their dimensions (58). If the maximum shear stress exceeds the interfacial shear strength of the composite, immediate catastrophic debonding between the fiber and the matrix occurs.

Lawrence (30) has developed a theory taking partial debonding and the effect of frictional forces acting over the debonded portion of the interface into account. The interfacial frictional force along the debonded interface results from the existence of residual gripping pressure. The applied load should overcome this static frictional force along the debonded interface in addition to the force required for debonding the bonded regions of the interface. Using the same geometry of the model and the results as Greszczuk's, he discussed the maximum load (P_f^{max}) on the fiber required to achieve complete debonding and initiate pull-out from the matrix. He concluded that whether debonding continues at this load or an increase in load is necessary depends on the embedded length of the fiber (l_e) and the ratio of the interfacial shear strength (τ_i) to the frictional shear stress after debonding (τ_f) . In comparison with Greszczuk's results (Fig. 5), his conclusion is illustrated in Fig. 6.

Lawrence assumed that the interfacial frictional shear stress(τ_f) is constant over the debonded region. However, Takaku and Arridge (31) have pointed out that due to the Poisson's effect, the fiber contracts in the lateral direction under tensile stress. This contraction reduces the compressive stress from the matrix, and consequently the interfacial frictional force decreases. Although they have noticed such behavior of interfacial frictional stress, they, like Greszczuk, did not take the contribution of frictional shear stress along the debonded interface to their maximum load



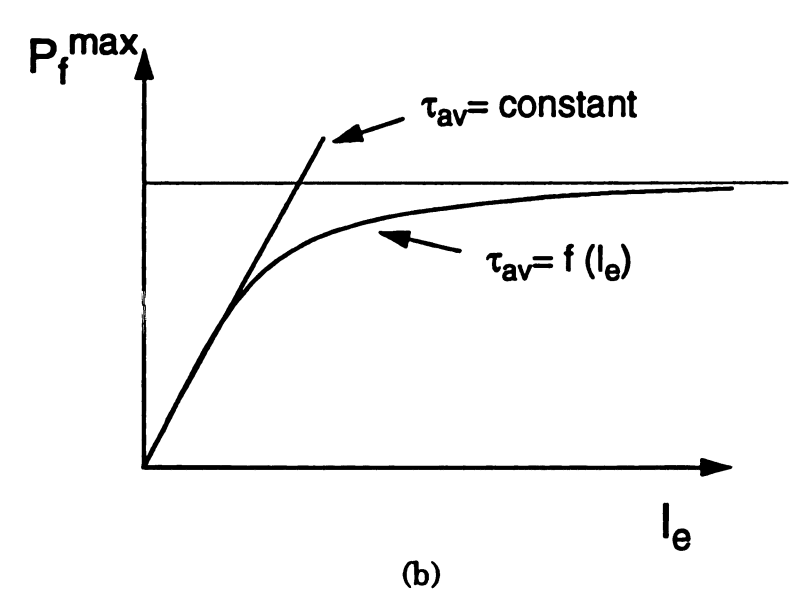
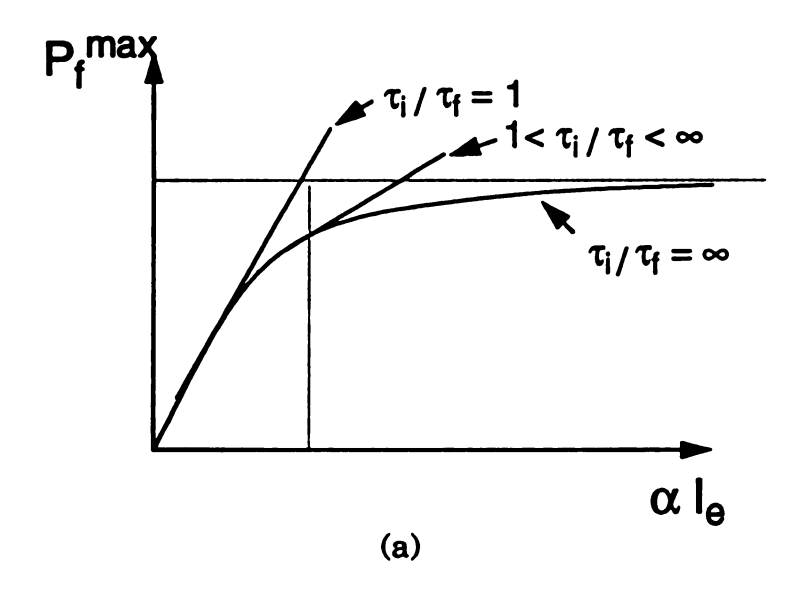


Fig. 5 (a) Variation in average interfacial shear stress with embedded fiber length. (b) Variation in maximum pull-out load with embedded fiber length [from Greszczuk (29)].



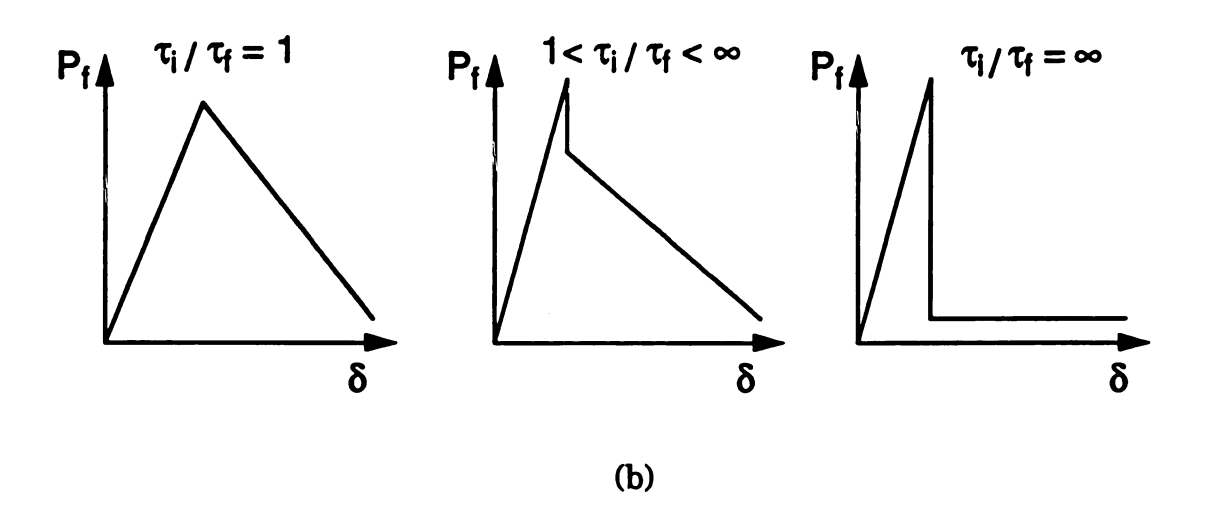


Fig. 6 Variation of maximum pull-out load (a) as a function of embedded fiber length, and (b) as a function of fiber displacement, for various friction conditions [from Lawrence (30)].

required to debond into consideration, and assumed that the debonding process is catastrophic as soon as the maximum shear stress exceeds the interfacial bonding strength. Instead they have derived the pull-out stress after complete debonding has occurred, in consideration of the decrease of the frictional stress due to Poisson contraction of the fiber under tensile stress. The initial pull-out stress is given by

$$\sigma_i = A \left(1 - \exp \left(-Bx_e \right) \right) \tag{Eq. 3}$$

where x_e is the embedded length of the fiber, A is a function of the normal compressive stress exerted by the matrix on the fiber across the interface and the elastic properties of the fiber and the matrix, and B is a function of the coefficient of friction between the fiber and matrix at the interface, and their elastic properties.

Bowling and Groves (59) have developed a model for the debonding and pull-out of a ductile fiber embedded in a brittle matrix. They followed a theoretical treatment of the debonding stress proposed by Outwater and Murphy (60), based on an energy balance argument:

$$\sigma_d = \sqrt{\left(\frac{8E_f\gamma}{r_f}\right)} + \frac{2\tau_f l_d}{r_f}$$
 (Eq. 4)

where E_f is the Young's modulus of the fiber, r_f is its radius, τ_f is the frictional shear stress in the debonded region, γ is the fiber-matrix interfacial energy and l_d is debonded length of the fiber. According to their model, at a sufficiently large value of l_d , the debonding stress exceeds the yield stress of the fiber and the relatively large plastic radial contraction of the

fiber reduces the frictional shear stress in the debonded region to zero.

Therefore, they have concluded that debonding stress is independent of the embedded length and is determined by the yield stress and work-hardening rate of the fiber and roughness of debonded surfaces.

A graphical interpretation and analysis of pull-out test results for ductile fibers embedded in a brittle matrix was proposed by Bartos (32), and Lawrence's theory was extended to calculate the load-displacement curve during pull-out, the crack spacing and strength of aligned short fiber composites by Laws (46). Recently Hsueh (35) has provided rigorous solutions for stresses required to debond the fiber/matrix interface and to pull-out a fiber in a manner similar to shear-lag analysis incorporating shear deformation in the matrix.

Several approaches have been used to analyze the interfacial shear stresses in push-out configurations (44,55,57,61-69), since the development of an indentation method for measuring frictional stresses at interface in ceramic matrix composite by Marshall. In Marshall's calculations of sliding frictional stresses at the interfaces based on an energy balance analysis (55), it was assumed that the interfacial shear stress over the embedded length is uniform, and consequently the influence of Poisson expansion of the fiber on the frictional shear stresses at interfaces was neglected.

Grande et al. (44) have analyzed the fully bonded fibers in push-out tests using finite-element method, providing a more accurate modelling of the localized point loading at the free fiber. A modified shear-lag analysis for the push-out tests has been proposed by Shetty (61). The Poisson expansion of the fibers under the compressive loads and the consequent increase of the normal stress across the interface leads to a nonlinear variation of the frictional shear stress along the embedded fiber length. Weihs et al.

(64,65) have attempted to incorporate Marshall's energy balance analysis with Shetty's consideration of Poisson expansion of the fiber.

In addition, the importance of roughness of debonded surfaces to the frictional shear stress at the interface was considered by several researchers (53,70,71) who have modelled its effect as an addition to the clamping pressure causing interfacial frictional shear stress. A detailed analysis of asperity interactions was presented by Carter et al. (70). Roughness is modelled as Hertzian contacts, leading to a sinusoidal modulation of the sliding pressure. Kerans et al. (53) included asperity pressure due to roughness of the interface in their treatment of clamping pressure, and have provided a discussion of abrasion during fiber sliding. Most recently Mackin et al. (71) developed a model considering an elastic asperity mismatch at the interface resulting in an asperity pressure at the interface and incorporating fractal models of interface roughness.

2-2. Fracture Toughness Measurements in Ceramic Matrix Composites

Ceramic matrix composites exhibit dramatic improvement in toughness compared with monolithic ceramics. Nevertheless, due to the difficulty in defining representative and universal characteristics of crack propagation arising from crack front deflection, crack wake delamination and crack bridging, it is hard to provide a meaningful technique to measure mechanical properties of fiber-reinforced ceramic matrix composite. A number of researchers have proposed various techniques of fracture toughness measurements in ceramic matrix composites (1-28,72-76).

Single notched beam loaded in three point or four point bending is com-

monly used for fracture toughness measurement of ceramic matrix composites (2-4,18,19). Such measurements are based on the linear elastic fracture mechanics, which assumes the same mechanical behavior over the whole sample and the occurrence of a very small process zone in the vicinity of the crack tip. The critical stress intensity factor (fracture toughness) for single notched beam in three point bending is given by (77)

$$K_{Ic} = Y \frac{6M_{max}a^{\frac{1}{2}}}{BW^2}$$
 (Eq. 5)

where M_{max} is applied bending moment at peak load, B is the thickness of the specimen, W is the width of the specimen, a is initial crack length, and Y is a geometry factor which is a function of a/W. However, as observed by Marshall $et\ al$. (78), debonding along the interface is accompanied with crack propagation normal to the fibers during failure of the ceramic matrix composites unidirectionally reinforced with fibers. Therefore, measurement of fracture toughness by flexural tests on the linear elastic fracture mechanics basis becomes invalid (78,79). In addition to this, the pull-out effect is not included in this analysis because the behavior after peak load is neglected. However, this technique may be applicable to ceramic matrix composites reinforced with particles, assuming isotropic behavior of the material due to uniform dispersion of small size particles.

Several recent studies have dealt with J-integral method for analyzing the toughening due to crack bridging in ceramic matrix composites (5-8,10-13,21-25,73,74). J-integral method developed by Rice (80) provides a solution for considerable mathematical difficulties encountered in determination of concentrated strain fields near crack tip in nonlinear elastic

materials. Path independent J-integral is defined by

$$J = \int_{\Gamma} \left(w dy - \left(\overline{T} \cdot \frac{\partial \overline{u}}{\partial x} \right) ds \right)$$
 (Eq. 6)

where Γ is a curve surrounding the crack tip, ω is the strain-energy density, \overline{T} is the traction vector defined according to the outward normal along Γ , \overline{u} is the displacement vector and ds is an element of arc length along Γ . J is equal to the strain energy release rate as calculated from the usual continuum solution for small-scale yielding. Employing path independent J-integral in Dugdale-Barenblatt crack model (81) shown in Fig. 7, with dy=0 on Γ , Eq.6 can be written as

$$J = \int_0^{\delta_t} \sigma(\delta) \, d\delta \tag{Eq. 7}$$

where δ_t is the separation distance at the crack tip. Some researchers evaluated the fracture toughness due to crack bridging by intact fibers in ceramic matrix composites using J-integral method with same concept as Dugdale-Barenblatt crack model (Eq. 7) and obtained

$$\Delta G_c = J_c = V_f \int_0^{u^*} \sigma(u) \, du. \tag{Eq. 8}$$

where ΔG_c is the critical strain energy release rate, V_f is the area-fraction of reinforcement intercepted by the crack, $\sigma(u)$ is the normal stress acting on the reinforcement, and u^* is the crack opening at the point where reinforcement fails. However, if the crack opening distance in the crack bridging zone is relatively large due to weak bonding, then dy in Eq. 6 can not be

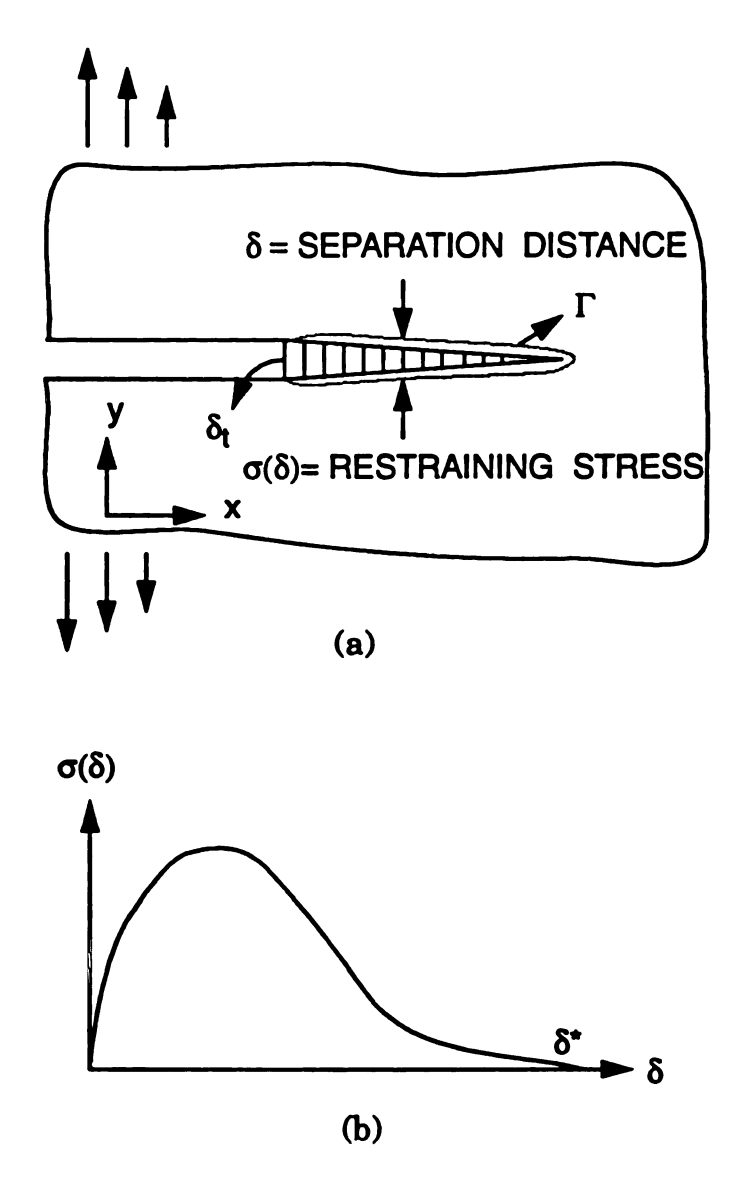


Fig. 7 Dugdale-Barenblatt crack model (81). (a) Cohesive zone at crack tip with restraining stress dependent on separation distance; (b) force-displacement relation for atomic attraction in elastic brittle fracture.

considered as zero, and consequently Eq. 7 can not be obtained in this case. Therefore, J-integral method does not seem to be an appropriate method to evaluate the fracture toughness of ceramic matrix composite, especially with metallic fiber-reinforcement. However, taking only the result of this approach into account, Eq. 8 represents the strain energy release rate due to crack bridging by intact reinforcements.

2-3. Strength Analyses in Ceramic Matrix Composites

Many ceramic matrix composites in which the failure strain of the matrix is less than that of the fiber experience cracking of the matrix when subjected to a uniform stress in the fiber direction. A critical stress at which the composite displays first evidence of the matrix cracking is called first matrix cracking stress. The first matrix cracking can cause damage to mechanical behavior of the composites. First of all, matrix cracking reduces the elastic modulus of the composite. Moreover, the intact fibers are exposed to oxidizing environment due to such cracks resulting in strength deterioration of the composite at elevated temperatures. Therefore, the first matrix cracking stress can be considered as a design stress in many applications of the composites at elevated temperatures. A number of micromechanical models which relate the first matrix cracking stress to composite parameters have been developed (82-88).

Aveston, Cooper and Kelly (ACK) (82) have analyzed the mechanism of matrix fracture in fiber-reinforced brittle matrix composites with frictionally coupled interface. Their approach was based on an energy balance criterion under steady state cracking. According to this analysis, the matrix failure strain of the composite, ε_{muc} , will be enhanced only when

$$\varepsilon_{mu} < \left\{ 12\tau \gamma_m \left(\frac{V_f^2}{rV_m} \right) \left(\frac{E_f}{E_c E_m^2} \right) \right\}^{1/3}$$
 (Eq. 9)

where ε_{mu} is the normal failure strain of the monolithic matrix, τ is the fiber/matrix interface shear strength, γ_m is the matrix fracture energy, r is the fiber radius, and E_f , E_c and E_m are the Young's moduli of the fiber, composite and matrix, respectively. As long as the condition in Eq.9 is satisfied, ε_{muc} increases with variation in composite parameters. On the other hand, as mentioned by Davidge (84), when the inequality in Eq. 9 is not obeyed, the matrix failure strain in the composite will be equal to the failure strain of the monolithic matrix, i.e. $\varepsilon_{mu} = \varepsilon_{muc}$. Further increase in strain results in matrix cracks normal to the fibers.

Budianski, Hutchinson and Evans (BHE) (83) have treated both frictionally and adhesively coupled interfaces and studied the matrix cracking stress in a more rigorous fashion. They concluded that in the Coulomb friction-operative case, the larger strain mismatch would not lead to the higher matrix cracking stress, despite the larger frictional resistance available. This is due to the fact that the same strain mismatches also lead to axial tensile stresses in the matrix which act to reduce the matrix cracking stress. Therefore, optimal strain mismatches exist for maximizing the matrix cracking strength. On the other hand, in the case of initially bonded fibers, the matrix cracking stress would increase with interface bonding toughness. More recently, Sutcu and Hillig (SH) model (86) also included the effect of both the adhesion and friction on the first matrix cracking stress, considering axial tensile stress to cause debonding. Each of these models assumed a steady-state matrix cracking and predicted dependence of the first matrix cracking stress on the interfacial shear

strength in brittle matrix composite.

Singh (87) has recently compared the theoretical predictions of these models with experimentally observed values of matrix cracking stress in ceramic matrix composite. According to his experimental results, the matrix cracking is controlled by the critical strain for matrix cracking rather than the interfacial properties. He concluded that his results did not agree with the prediction of energy-based models such as ACK, BHE and SH models, but appeared to be in good agreement with a strain-based model suggested by Davidge (84).

In addition to the first matrix cracking stress, the ultimate load-carrying capacity of the composite is of interest as well. Schwietert et al. (88) have presented a theory for computing the ultimate tensile strength of fiber-reinforced composites with multiple matrix cracking, considering the distribution of fiber breaks and their contribution to the diminished load-carrying capacity of the composite. They concluded that the strength of the composite depends sensitively on the interfacial shear stresses and on the fiber strength variability.

3. Experimental Procedure

The composite specimens were fabricated by sandwiching technique (89) using as-received or acid-etched ribbons. The ribbon geometry for reinforcement was selected to facilitate the ease of fabrication and theoretical modelling of the composite. Acid etching of the ribbon, in as-received or pre-oxidized conditions, was performed in order to modify the interfacial characteristics of the composite (42). Interface modification was also carried out by thermal cycling the composite specimens reinforced with as-received ribbon for various numbers of thermal cycles (41); the maximum temperature of the thermal cycles was also changed to achieve different thermal stress conditions. Pull-out tests of the specimens in various bonding conditions were carried out to evaluate the interfacial bonding strength. The fracture toughness of the composites was measured by three point bending test using single notched beam specimens, and by tensile testing pre-cracked specimens (22).

3-1. Materials

The matrix material used in this study was soda-lime slide glass (73 wt% SiO_2 - 15 wt% Na_2O - 4 wt% MgO - 7 wt% CaO - 1 wt% Al_2O_3). The dimensions of this slide glass was 76.2mm x 25.4mm x 1.1mm. Nichrome ribbon (80 wt% Ni - 20 wt% Cr) was chosen as the reinforcement. The Nichrome ribbons were 1.5 ~1.8mm wide and 80 μ m thick. Tensile properties of a Nichrome ribbon with same heat treatment conditions as involved in the composite fabrication (450°C for 1 hour, and then 710°C for 3 hours)

was determined by Instron testing machine. The tensile stress-strain curve of the Nichrome ribbon used is shown in Fig. 8. The mechanical and physical properties of the matrix and ribbon used in current study are shown in Table 1.

3-2. Composite Fabrication

Specimens were fabricated by sandwiching a series of aligned ribbons between the glass slides (89), as shown in Fig. 9. Prior to sandwiching the ribbons, the glass slides and Nichrome ribbons were cleaned with acetone and rinsed in distilled water. To avoid misalignment of the glass slides and ribbons during loading of the specimen into the furnace, a small amount of epoxy glue was applied to the corners of the glass slides. A pair of stainless steel plates (100mm x 40mm x 1.5mm), one as the base plate on which the specimen is placed inside the furnace, the other as cover plate on which the weight is applied, were utilized. A stainless steel block (100mm x 35mm x 10mm) (0.75 lbs) was used as a weight to achieve good contact between the matrix and the ribbon. The stainless steel plates were coated with BN spray in order to avoid sticking to the samples and to prevent their oxidation during fabrication.

The composite fabrication involved two steps of heating: 450°C for 1 hour and 710°C for 3 hours. The low temperature step avoided gas trapping at the interface regions of the composites resulting from outgassing of the epoxy glue during fabrication. The high temperature step, which used a temperature of 10°C higher than the softening temperature of soda lime glass, allowed the glass to flow and cause adherence to the reinforcements. The weight (stainless steel block), and the top stainless steel plate were

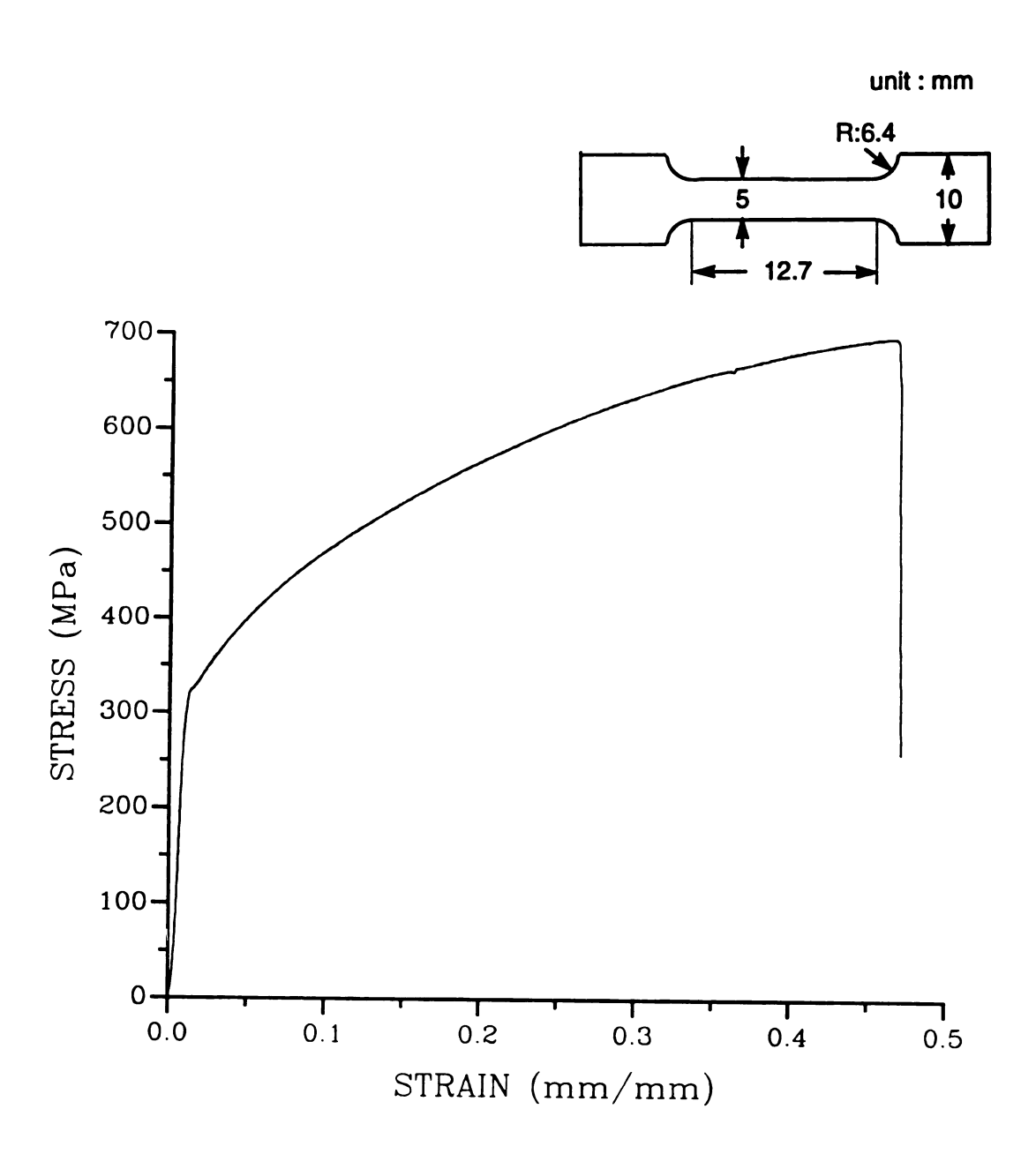


Fig. 8 Typical stress-strain curve of the Nichrome ribbon obtained from tensile test.

Table 1: Physical and mechanical properties of constituents of the composite

	Matrix	Ribbon
	soda lime	
Material	slide glass	Nichrome
Thermal Expansion Coefficient (10 ⁻⁶ /°C), (25 °C ~ 500 °C)	9.2	14.3
Young's Modulus (GPa)	72	213
Yield Strength (MPa)		305
Tensile Strength (MPa)		700
Softening Temperature (°C)	700	

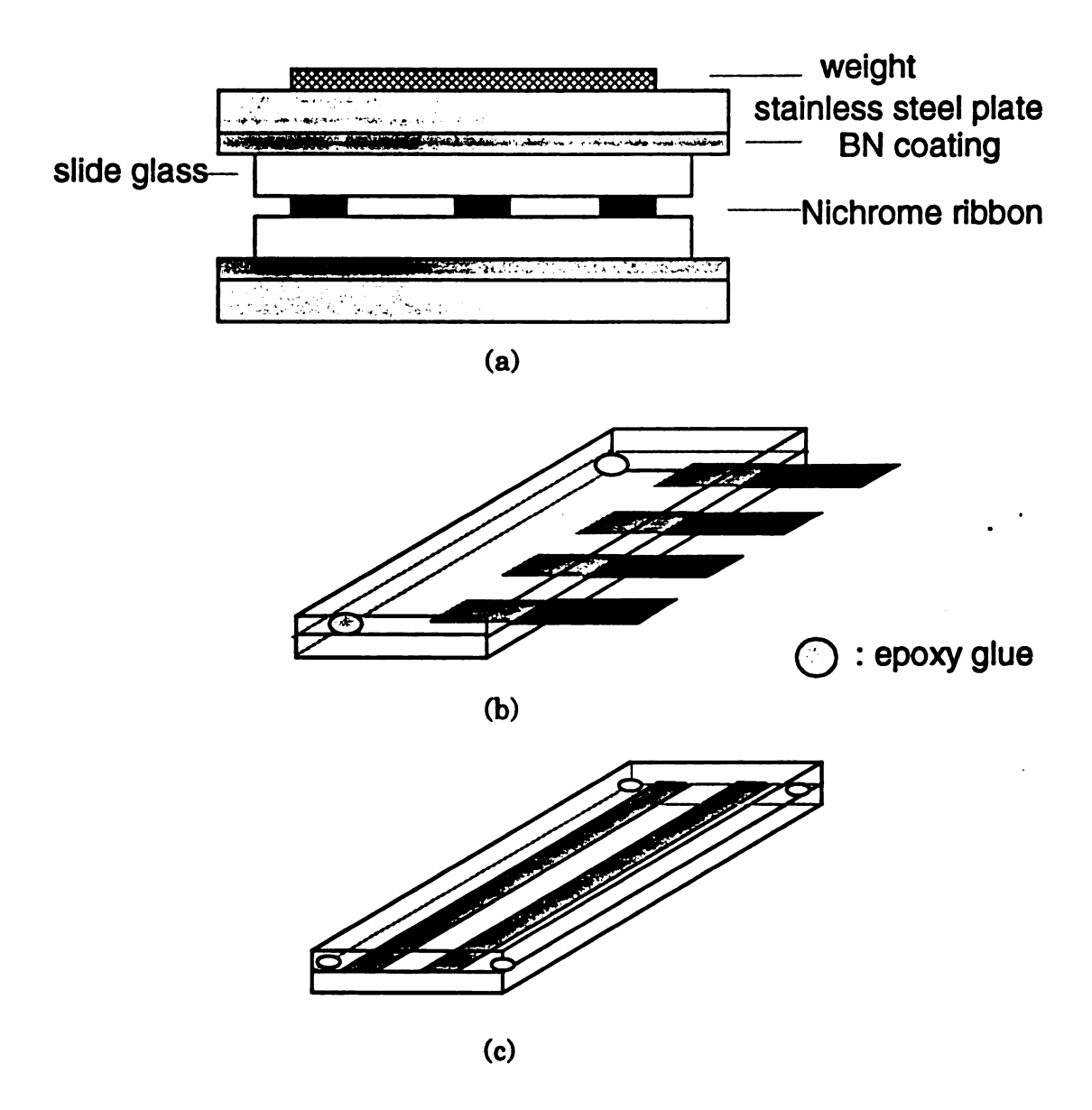


Fig. 9 The schematics illustrating sandwiching of a series of aligned ribbons between the glass slides: a) general set-up, b) composite from which pull-out test samples were cut out, and c) composite from which fracture toughness test samples were cut out.

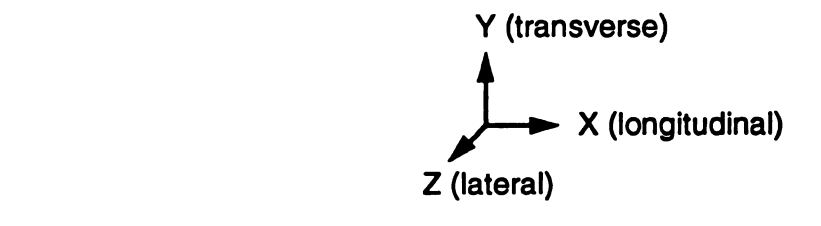
removed after cooling to 500°C. The composites were annealed at 500°C for 2 hours, then cooled to room temperature in the furnace. Entire composite fabrication was carried out in ambient atmosphere.

Pull-out specimens (4mm x 10mm x 15mm) and fracture toughness test specimens (5mm wide and 6mm thick) were cut out from the fabricated composite stocks using a low speed diamond saw. The schematics of typical pull-out and pre-cracked tensile specimens are shown in Figs. 10 and 11 respectively. The composite specimens cut to proper dimensions were mechanically polished with a series of abrasive grit papers ranging from 240 grit to 600 grit.

3-3. Interface Modification

3-3-1. Thermal Cycling Technique

Thermal cycling method used in this study involved placing the specimens on a platform in the center of a standard laboratory furnace (Lindberg) at various temperatures for 3 hours, followed by cooling in still air and holding at room temperature for 3 hours. The maximum temperatures used for thermal cycling were 500, 550, 600, and 650°C. These temperatures lie between the strain temperature (480°C) and softening temperature (700°C) of soda lime glass. These thermally cycled specimens are referred to as 500-TC, 550-TC, 600-TC, and 650-TC specimens in this study. The number of thermal cycles chosen in this study were 3, 5, and 7 cycles for each maximum cyclic temperature.



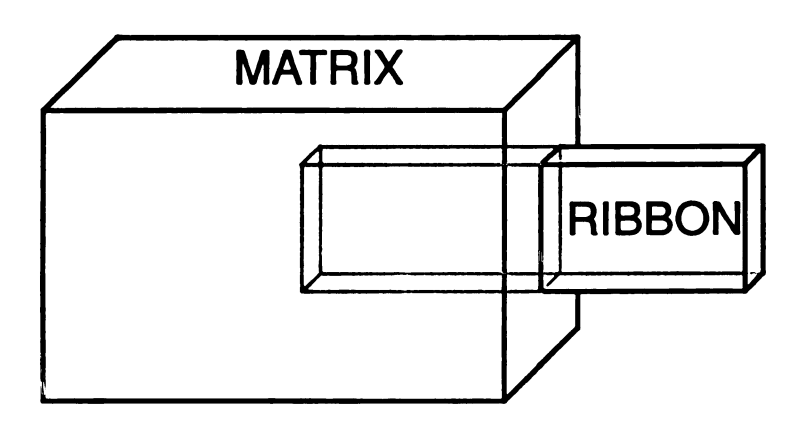


Fig. 10 The schematic of typical pull-out specimen.

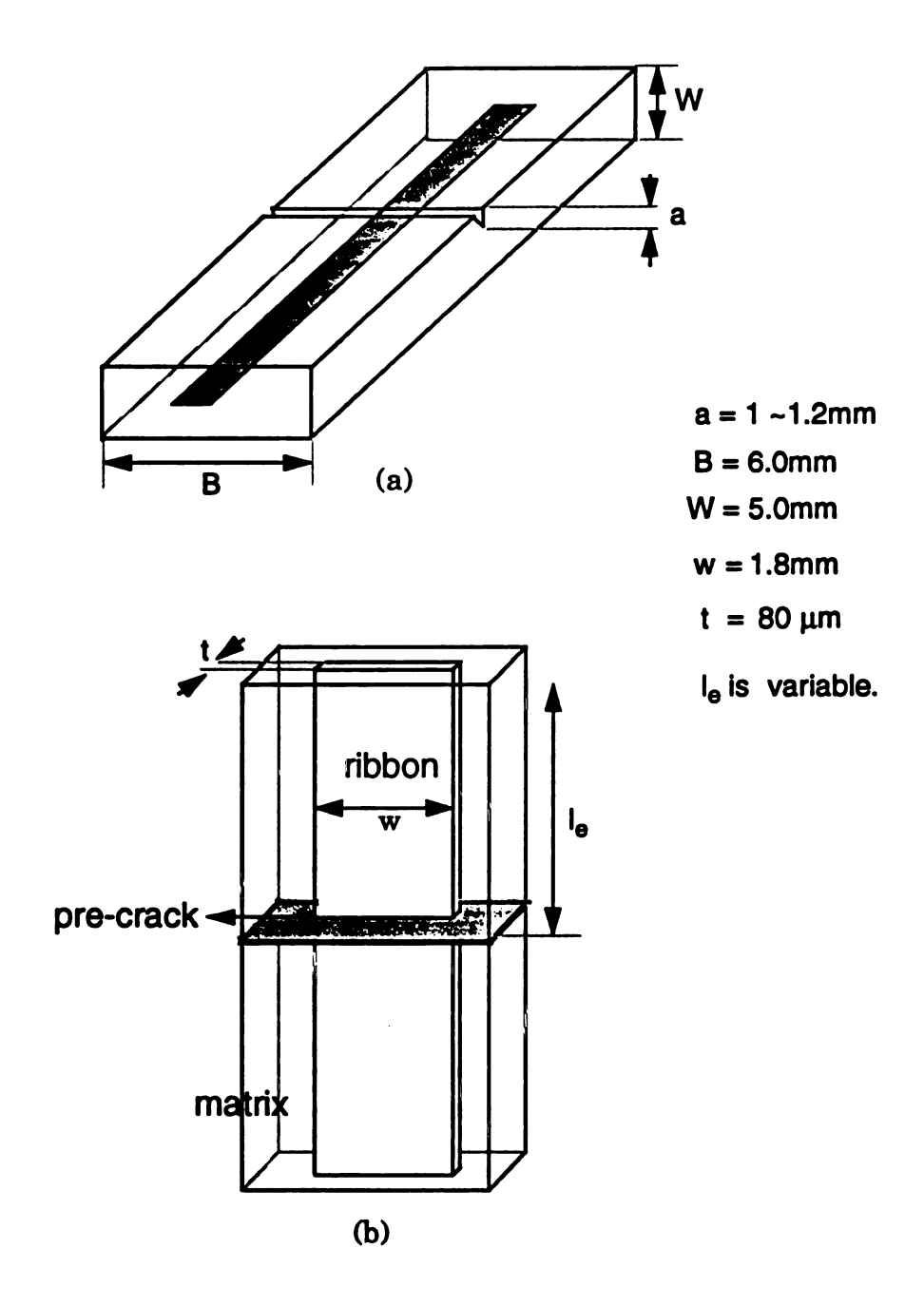


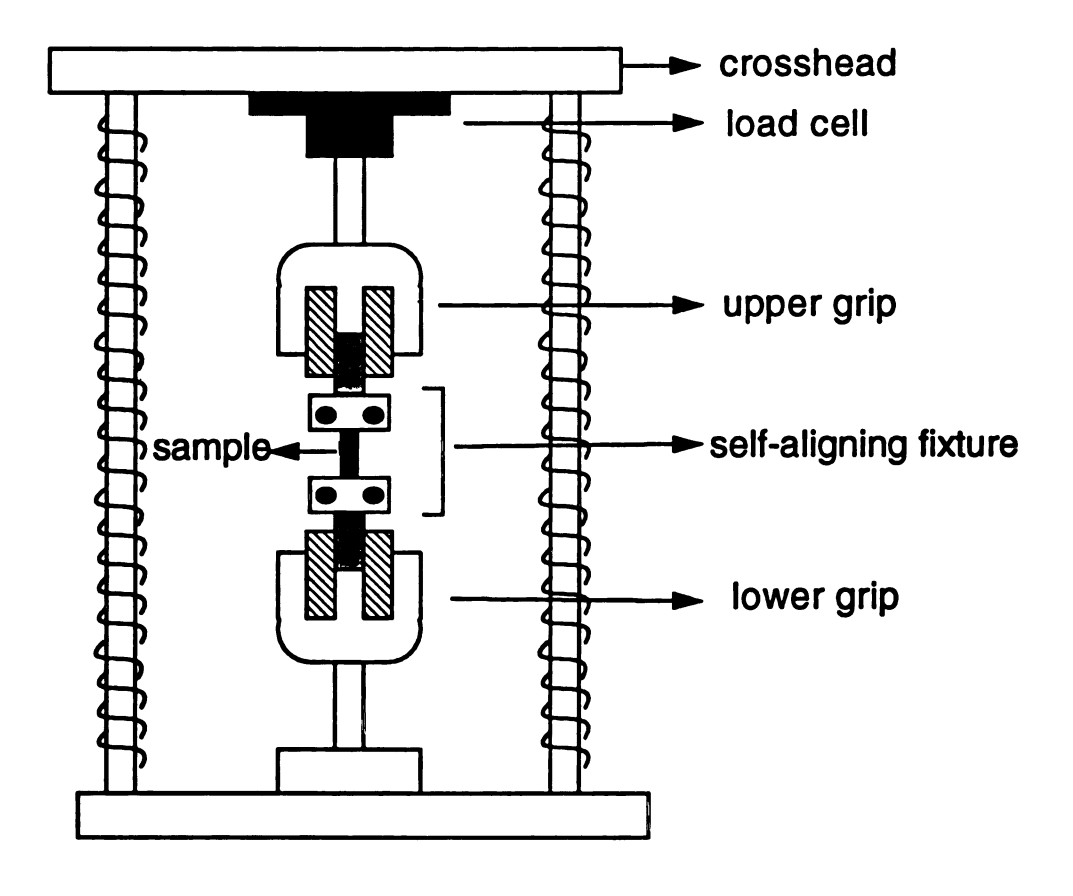
Fig. 11 The schematic of typical fracture toughness test specimens:
a) single notched specimen for flexure test, and b) precracked specimens for tensile test.

3-3-2. Acid Etching Technique

Prior to the composite fabrication, the surfaces of Nichrome ribbons were etched in order to modify the interfacial characteristics of the composites. The ribbons in both as-received and pre-oxidized conditions were acid etched. Pre-oxidizing of the ribbon involved holding the Nichrome ribbons (cleaned with acetone and rinsed with the distilled water) at 650°C for 1 hour. The oxide layer produced by such a step reduced the intensity of acid etching on the ribbon surfaces. The Nichrome ribbons, in both conditions, were etched with a solution of 20% HNO₃ and 80% HCl for various lengths of time: 5, 15, 30, 60 and 90 seconds.

3-4. Mechanical Testing

Pull-out tests were carried out on the composite specimens with various interfacial bonding conditions to evaluate the interfacial bonding characteristics. These tests were conducted on a computer controlled Instron testing machine (model#4206), with a specially designed self-aligned fixture. The crosshead speed used was 0.5mm/min. For effective tensile gripping, the glass part of the specimen was held by glass-fiber reinforced epoxy tabs which was glued to the fixture (90). The glass fiber-reinforced epoxy tabs were used to prevent the cracking of glass matrix during tightening of the sample to the fixture. In addition, a dab of glue was also applied to the glass part of the specimen, before putting it on the fixture, to avoid slippage during pull-out test. The schematic of the experimental setup for the tensile test is shown in Fig. 12.



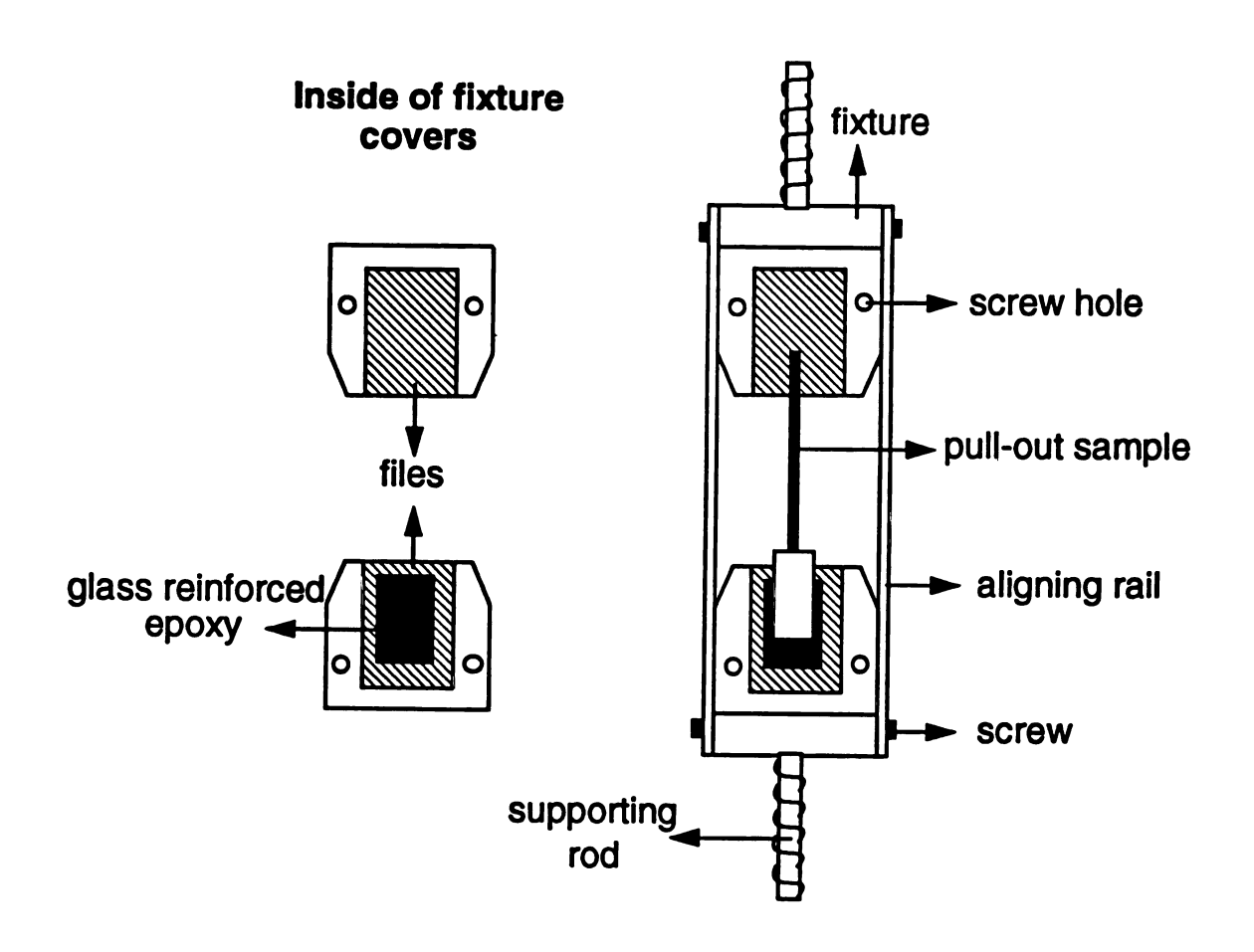
(a)

Fig. 12 A schematic of the experimental set-up for the tensile test:

a) general set-up, b) self-aligning fixture. The aligning rails

were removed after positioning the specimen in the testing

machine.



(b)

Fig. 12 (continued)

Fracture toughness behavior of the composite was evaluated by both flexure and tension tests on the same specimen. The tension tests were carried out on pre-cracked specimens resulting from the flexure tests. The length of the specimens was varied from 20mm to 30mm. For flexure test, the composite specimens (5mm wide and 6mm thick) were initially notched by a slow speed diamond saw at the center of the specimen. Since diamond saw provides a blunt notch, a razor blade was used to produce a sharper notch at the base of the blunt notch. The resulting depths of the notches were measured after tension tests. Those values ranged between 1mm-1.2mm. These single notched specimens were loaded on a three point bending fixture with a 18mm span in an Instron testing machine. The crosshead speed was 0.2mm/min. Bending of the composite specimen was continued until the matrix cracked, as indicated by a drop in load. Due to such a procedure, the specimen contained a continuous matrix crack around the Nichrome ribbon. A sketch of a pre-cracked specimen is shown in Fig. 11. Using values of the peak load obtained from three point bending tests, K_{1c} was calculated using linear elastic fracture mechanics (77). Tension tests were carried out with these pre-cracked specimens, in order to study the effect of crack bridging on the fracture toughness of the composite (22). A tensile testing machine (Instron) was used in these tests with a specially designed self-aligning fixture (Fig. 12). The crosshead speed was 0.5mm/min. The pre-cracked specimens were placed in the self-aligning fixture. The ends of the specimens (to be gripped) were held by glass-fiber reinforced epoxy tabs which were already glued to the fixture. In addition, a dab of glue was also applied to the ends of the specimen (to be gripped) before putting it on the fixture. The stress-displacement curves were

obtained using the Instron testing machine at a crosshead speed of 0.2mm/min. The areas under the curves were measured, and the values of the fracture toughness due to crack bridging were calculated by using Eq. 8.

3-5. Micrographic Observation

For the interfacial studies using SEM, the specimens were cut perpendicular or parallel to the specimen length with a low speed diamond saw. The cut samples were mounted in lucite and mechanically polished with a series of abrasive grit papers ranging from 240 grit to 600 grit followed by polishing on cloth using 5µm to 0.3µm size alumina powder abrasives. The polished specimens were etched with a solution of 20% HNO3 and 80% HCl for 20 seconds. Fractographic observations were made on the specimens fractured during tensile loading, using the Olympus stereo optical microscope equipped with two fiber-optic transmitted light sources. The directions of light sources were changed until a interference fringe pattern representing the crack path could be observed.

4. Results and Discussion

4-1. Theoretical and Experimental Analysis of Debonding Process of Ductile Ribbon Embedded in Brittle Matrix

4-1-1. Theoretical Modelling

Several analytical models of debonding process during fiber pull-out in fiber-reinforced ceramic matrix composites have been developed (29-36). Among these, the model suggested by Lawrence (30) was adopted in this study for elastic behavior of the sample shown in Fig. 8. The ribbon geometry of the reinforcement was used in this study so as to simplify the modelling and to achieve easy fabrication of composites. The distribution of shear stress (τ) along the interface at a point with a distance x from the embedded end of the ribbon due to applied load (P) is given by (30)

$$\tau = \frac{P\alpha}{2(w+t)} \left(\frac{\cosh \alpha x}{\sinh \alpha l_e} \right)$$
 (Eq. 10)

where w and t are width and thickness of the ribbon respectively, l_e is embedded length of the ribbon, and α is a shear-lag parameter dependent on elastic properties of the matrix and the ribbon and on their dimensions (31). The maximum shear (τ_{max}) which is obtained at the boundary where the ribbon enters the matrix is

$$\tau_{max} = \frac{P\alpha}{2(w+t)} \coth \alpha l_e$$
 (Eq. 11)

Since the values of coth αl_e approach unity for larger values of l_e , τ_{max} can be considered to be independent of l_e for large values of l_e .

4-1-1. Load Required to Initiate Debonding

In ceramic matrix composite reinforced with metallic ribbon, the boundary where the ribbon enters the matrix is affected by plastic deformation of the unembedded region of the ribbon. Therefore, the shear stress due to plastic deformation of the ribbon as well as the shear stress due to shearlag analysis acts at the interface along the boundary between free and embedded areas of the ribbon. These shear stresses are shown in Fig. 13. For simplification of this modelling, this can be considered as a 2-dimensional model because the thickness of the ribbon is negligible compared to its width and length. Accordingly, the sketches in Fig. 13 illustrate long transverse faces of the specimens. The amount of shear stress that can contribute to debonding (τ_s) equals to the resolved shear stress available in excess to that required to initiate plastic deformation, and τ_s is assumed to act along a direction at 45° to the pull-out direction. This assumption can be explained by Hall-Patch model for deformation of polycrystals (91).

$$\tau_s = \tau_{rss} - \tau_{yrss} = \frac{\sigma}{2} - \frac{\sigma_o}{2} = \frac{P - wt\sigma_o}{2wt}$$
 (Eq. 12)

where τ_{rss} is resolved shear stress due to applied normal stress, τ_{yrss} is resolved shear stress required for yielding of the reinforcement, σ is applied normal stress, and σ_o is yield stress. τ_s is combined with τ_{max} to obtain the resultant shear stress (τ_t) at the interface along the boundary between free and embedded areas of the ribbon, so that

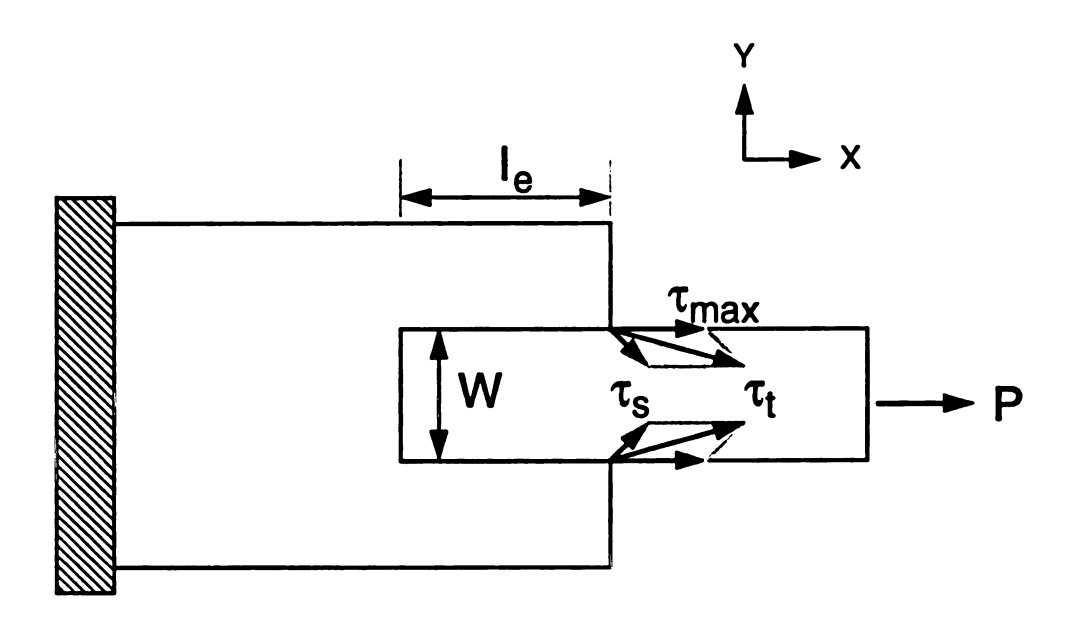


Fig.13 Shear stresses due to tensile loading at edge of the embedded area $[\tau_{max}$: shear stress obtained by modified shear lag model (30), τ_s : resolved shear stress available in excess to that required to initiate plastic deformation of the ribbon by slip, and τ_t : resultant shear stress due to τ_{max} and τ_s] Note: τ_s is at 45° to the direction of P.

$$\tau_t = \sqrt{\tau_{max}^2 + \sqrt{2}\tau_{max}\tau_s + \tau_s^2}$$
 (Eq. 13)

When resultant shear stress along the boundary between free and embedded areas of the ribbon (τ_t) exceeds the interfacial shear strength of the composite (τ_i) , interfacial debonding initiates. Therefore, the interfacial shear strength of the composite can be written as

$$\tau_i = \sqrt{(\tau_{max}^d)^2 + \sqrt{2}(\tau_{max}^d)(\tau_s^d) + (\tau_s^d)^2}$$
 (Eq. 14)

where superscript 'd' corresponds to debonding condition. Accordingly,

$$\tau_{max}^{d} = \frac{P^{d}\alpha}{2(w+t)} \coth \alpha l_{e} \quad and \quad \tau_{s}^{d} = \frac{P^{d} - wt\sigma_{o}}{2wt} \quad (Eq. 15)$$

where P^d is the load required to initiate interfacial debonding of the composite.

4-1-1-2. Load Required for Continuation of Debonding

After initiation of interfacial debonding, static frictional force (P_x^f) arises at the debonded interface due to residual gripping stress (σ_n) . This residual gripping stress is due to thermal expansion coefficient mismatch between the ribbon and the matrix (31). Therefore, in order to continue to debond, the applied load (P_x) should overwhelm this static frictional force as well as the load required to debond at the bonded/debonded boundary (Fig. 14).

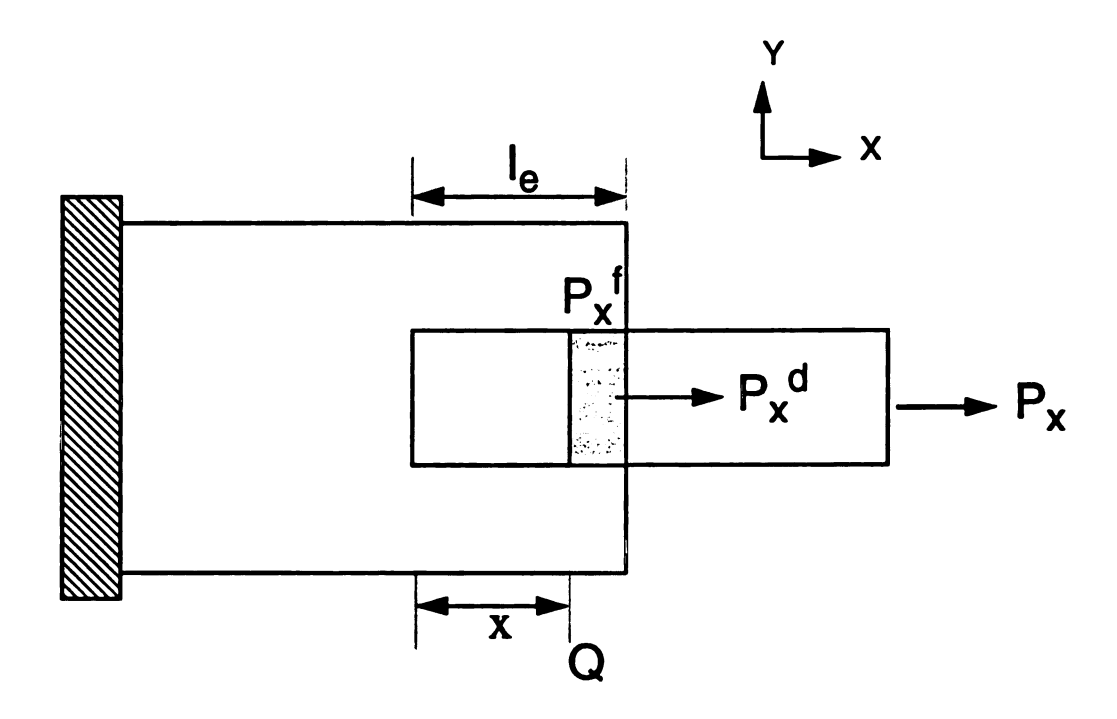


Fig.14 Load (P) required for continuation of debonding: $P_x > P_x^d + P_x^f$ where P_x^d is force required to debonding, and P_x^f is the frictional force between debonded region (shaded area) of ribbon with the matrix.

The load required to continue debonding at the bonded/debonded boundary (P_x^d) can be determined from (Eqs. 14 and 15) under the assumption that interfacial shear strength (τ_i) is uniform through the whole interface of the composite. At the location marked Q in Fig. 14, the debonded length is $(l_e$ -x), and the interfacial shear strength is

$$\tau_{i} = \sqrt{(\tau_{x}^{d})^{2} + \sqrt{2}(\tau_{x}^{d})(\tau_{s,x}^{d}) + (\tau_{s,x}^{d})^{2}}$$
 (Eq. 16)

where

$$\tau_x^d = \frac{P_x^d \alpha}{2(w+t)} \coth \alpha x, \quad and \quad \tau_{s,x}^d = \frac{P_x^d - wt\sigma_o}{2wt} \quad (Eq. 17)$$

The static frictional force (P_x^f) at the debonded interface can be determined in the following manner. Assuming coefficient of friction (μ) to be a constant throughout the debonded interface, frictional force change (dP_x^f) with infinitesimal change in distance (dx) at Q (Fig. 15) is

$$dP_x^f = 2(w+t)\mu\sigma_n dx$$
 (Eq. 18)

However, under external tensile loading, contraction of thickness of the ribbon due to elastic and plastic deformation reduces the gripping stress from the matrix, resulting in decreased frictional force. Reductions in the gripping stress from the matrix result from Poisson's effect due to elastic deformation by $k\sigma_r$ (31) and from slip due to plastic deformation by σ_s , where k is a constant depending on the elastic properties of the constituents of the composite, σ_r is normal stress at Q in the direction of the ribbon pull-out, and σ_s is a component of τ_s mentioned in previous section in the

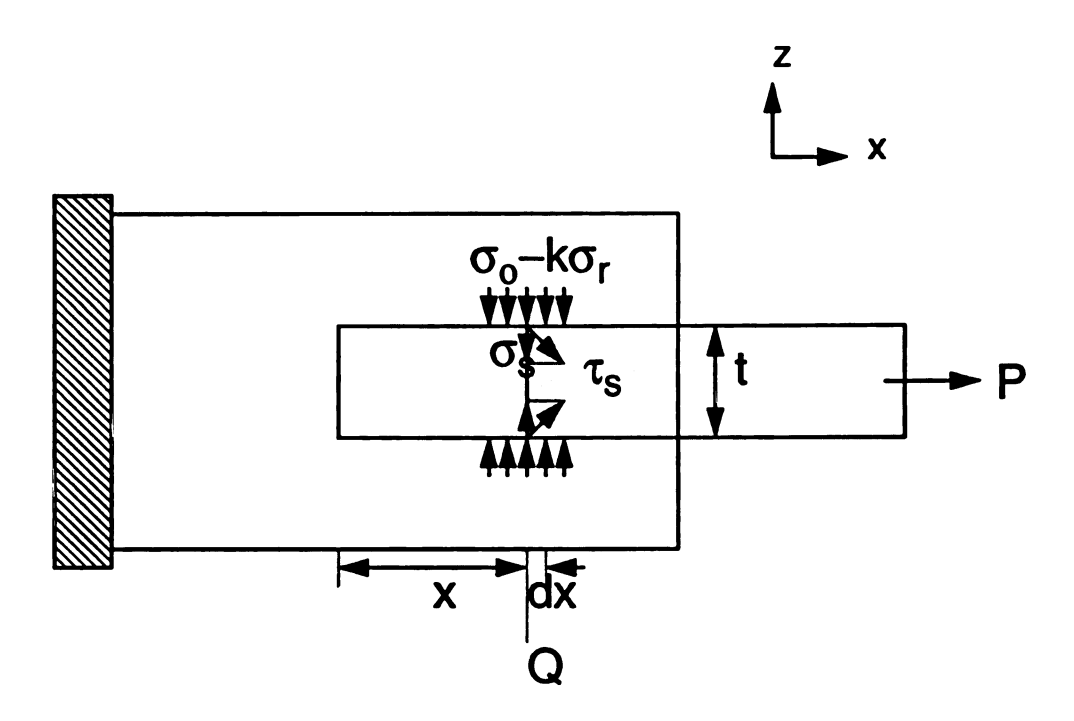


Fig.15 Static frictional force at the debonded interface: contraction of thickness of the ribbon due to elastic and plastic deformation reduces the gripping stress from the matrix.

thickness direction of the ribbon. Under such conditions Eq. 18 can be rewritten as

$$dP_x^f = 2(w+t)\mu(\sigma_n - k\sigma_r - \sigma_s)dx$$
 (Eq. 19)

 σ_r in this equation can be replaced by σ_o since the ribbon would have yielded under these conditions. The static frictional force at $Q(P_x^f)$ can be obtained by substitution of σ_r and σ_s , and by integration of Eq. 19 from l_e through x:

$$P_{x}^{f} = 2(w+t)\mu \int_{l_{*}}^{x} (\sigma_{n} - k\sigma_{o}) dx - \frac{(w+t)}{\sqrt{2}wt} \mu \int_{l_{*}}^{x} (P_{x}^{d} - wt\sigma_{o}) dx$$
 (Eq. 20)

In order to continue debonding, the applied load (P_x) should become

$$P_x > P_x^d + P_x^f \tag{Eq. 21}$$

Further plastic deformation of the ribbon after debonding is neglected in this analysis.

4-1-2. Experimental Analysis

A typical load-displacement curve obtained in pull-out test of the Nichrome ribbon embedded in soda-lime glass matrix is given in Fig. 16. In this test, the load linearly increases up to the point 'A', corresponding to the yield point of the ribbon. The free (unconstrained) area of the ribbon starts to deform plastically at point 'A', and work hardens on further deformation. This smooth work hardening curve is interrupted by small load

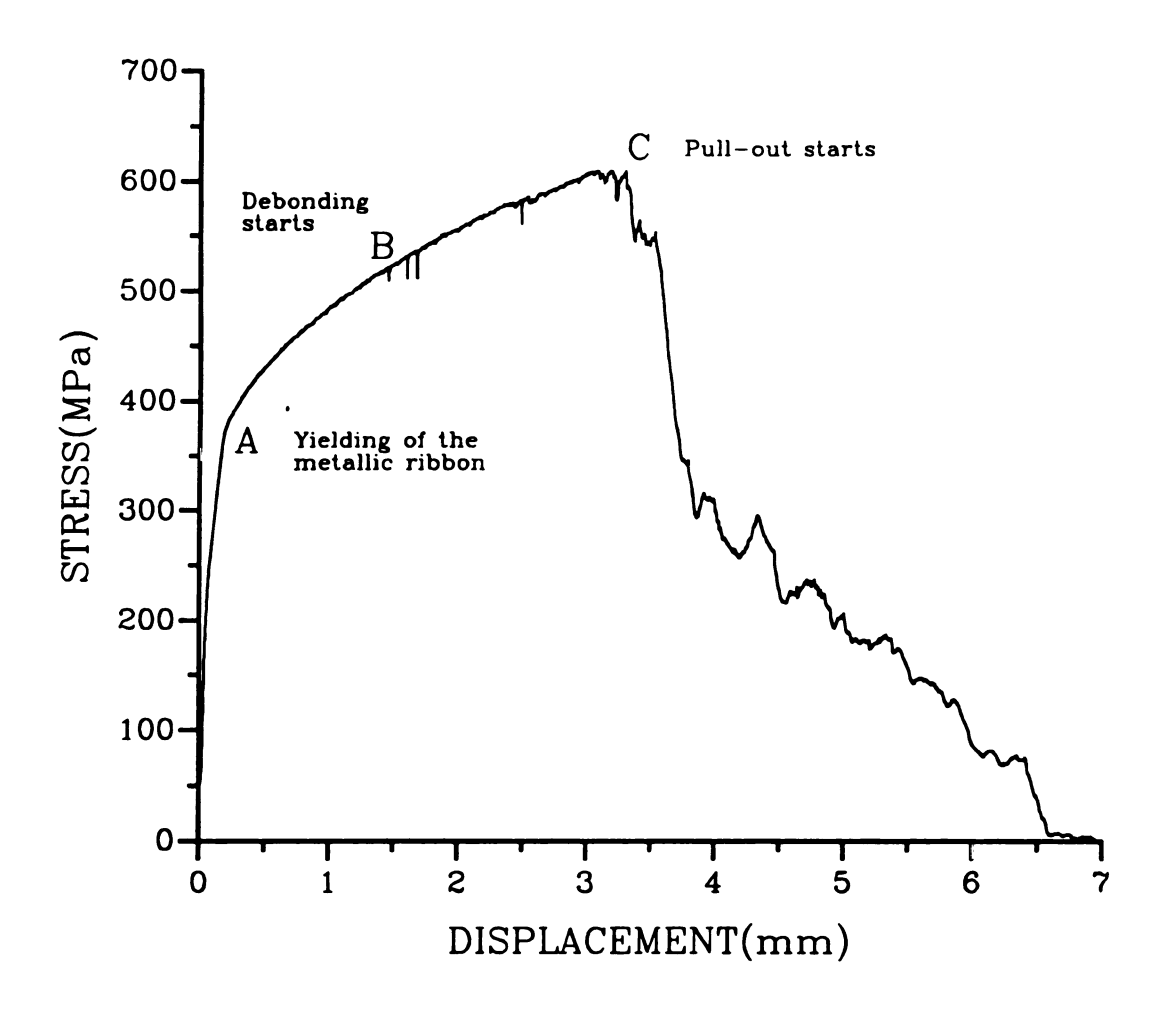


Fig.16 Typical stress-displacement curve obtained in pull-out tests of Nichrome ribbon embedded in soda lime glass matrix.

drops, and the first load drop 'B' is associated with initial debonding at the ribbon-matrix interface. As speculated by Morten et al. (90), the debonding front actually propagates in small jumps rather than continuously, accompanied by the small load drops on the load-displacement curve. After initial debonding, the load continuously increases as debonding progresses until the load reaches a peak point 'C'. At point 'C', complete debonding occurs along the full embedded length, and at the same time the ribbon pull-out initiates. The sudden load drop at this initiation of pull-out of the ribbon was not observed in this experiment. The explanation for this fact will be discussed in detail later. After initiation of pull-out, the load continuously decreases to zero until the ribbon is completely pulled out from the matrix.

SEM micrographs of the ribbon/matrix interface are shown in Fig. 17. A relatively thin oxide layer that can be seen at the interface facilitates chemical bonding between glass matrix and ribbon. The interface of this composite contains partially debonded regions due to the considerable mismatch in thermal expansion coefficients of the ribbon and the matrix. The crack was observed along the weak interface between the oxide layer and the Nichrome-metal. In this composite, the ribbon experiences tensile stresses in the lateral, longitudinal, and transverse directions due to the larger thermal expansion coefficient of the ribbon than that of the matrix. Therefore, once debonding occurs, the ribbon contracts not only in the lateral direction but also in both longitudinal and transverse directions. Considering dimensions of the ribbon, displacements due to longitudinal and transverse contraction of the ribbon are much larger than that due to lateral contraction. On the other hand, tensile loading during pull-out test gives rise to longitudinal plastic extension of the ribbon. As a result, longi-

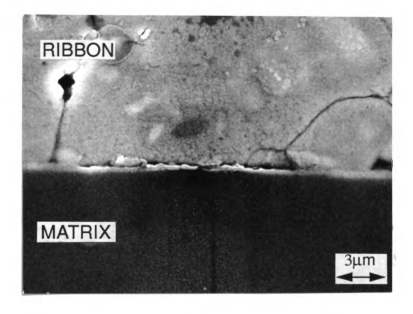


Fig. 17 SEM micrograph of the partially debonded interface between the Nichrome ribbon and the soda lime glass matrix

tudinal contraction of the ribbon due to release of the residual tensile stress by debonding vanishes and only plastic extension of the ribbon exists in the longitudinal direction. Consequently, transverse contraction and longitudinal plastic extension of the ribbon, coupled with the microscale roughness of the debonded surfaces, result in the mechanical keying of the debonded surfaces providing compressive stresses at the interface, as schematically shown in Fig. 18. The SEM micrograph of the interface between the ribbon and the matrix after debonding progresses to some degree is given in Fig. 19. To confirm progress of the debonding process, loading had been interrupted just before the ribbon can pull out from the matrix. The shear failure at the interface can be observed at the deep embedded location (M). It could have resulted from the plastic contraction in width of the ribbon as well as from the distribution of the shear stresses along the interface due to tensile loading. Although further plastic deformation of the ribbon after debonding was not considered in this analysis, this behavior was also indicated by increased crack opening of initially debonded location (N) in this figure.

The interfacial shear strength (τ_i) of this composite as a function of embedded ribbon length is shown in Fig. 20. These values of the interfacial shear strength of this composite were obtained by equations (14) and (15), using the results of load-displacement curves obtained experimentally. The interfacial shear strength of this composite was evaluated to be 97.9 ± 15.0 MPa. Plot of loads required to continue debonding as a function of debonded length, obtained on the basis of section 4-1-1-2, is given in Fig. 21. The load required for continuation of debonding (P_x) is the sum of the load required to debond at the bonded/debonded boundary (P_x^d) and static frictional force (P_x^f) . P_x^d gradually decreases with increasing debonded

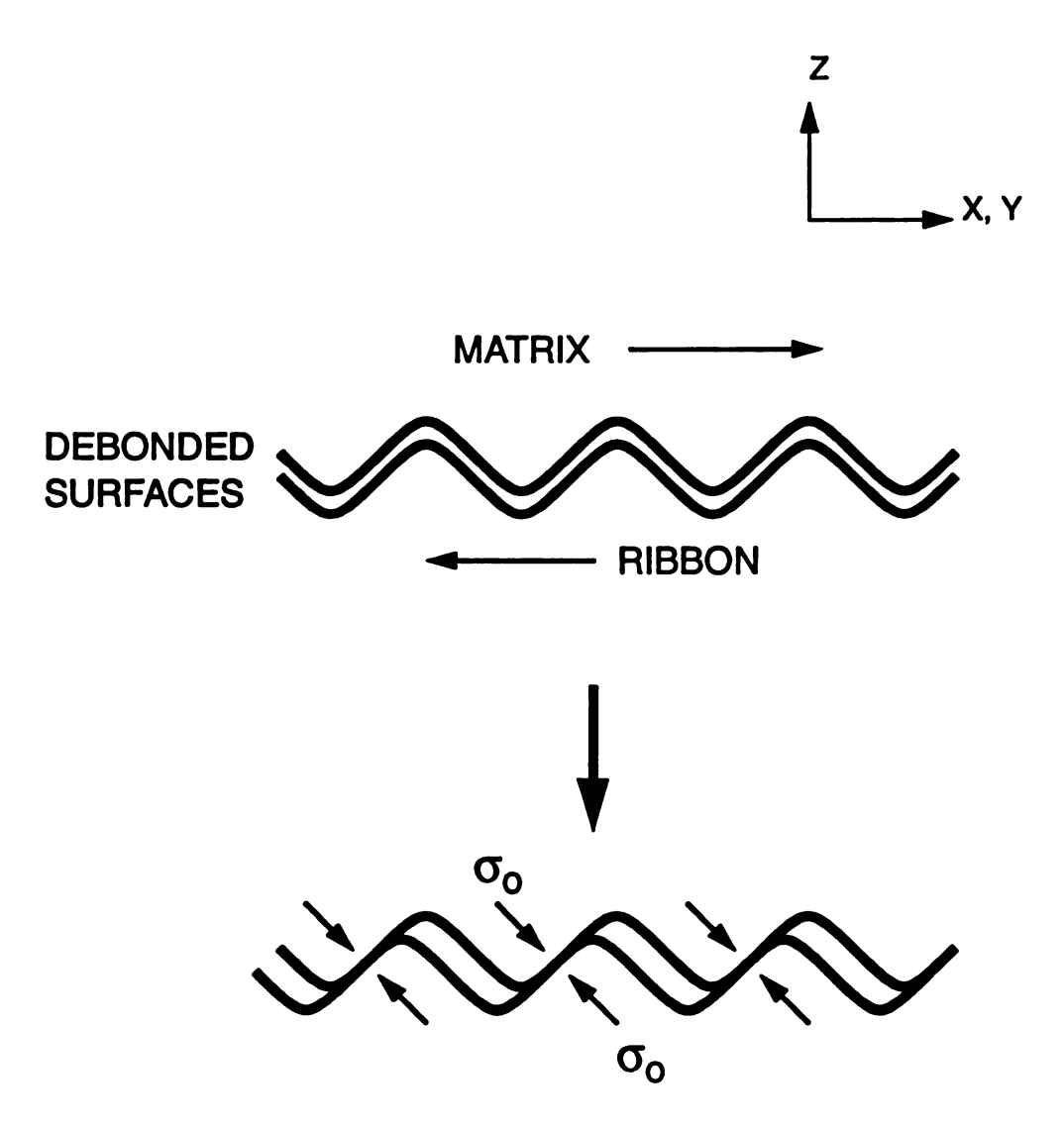


Fig.18 Mechanical keying of debonded surfaces produced by roughness of debonded surfaces, transverse contraction, and longitudinal plastic extension of the ribbon due to tensile loading after debonding.

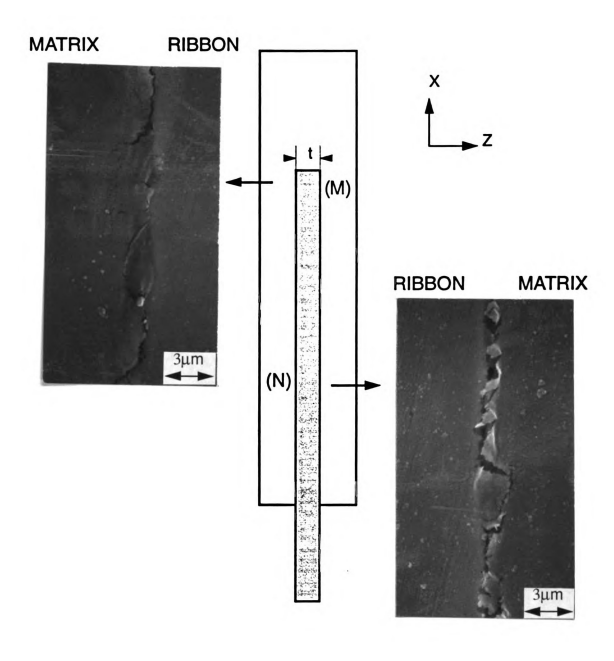


Fig.19 SEM micrograph of the interface between the Nichrome ribbon and soda lime glass matrix after debonding progresses to some degree

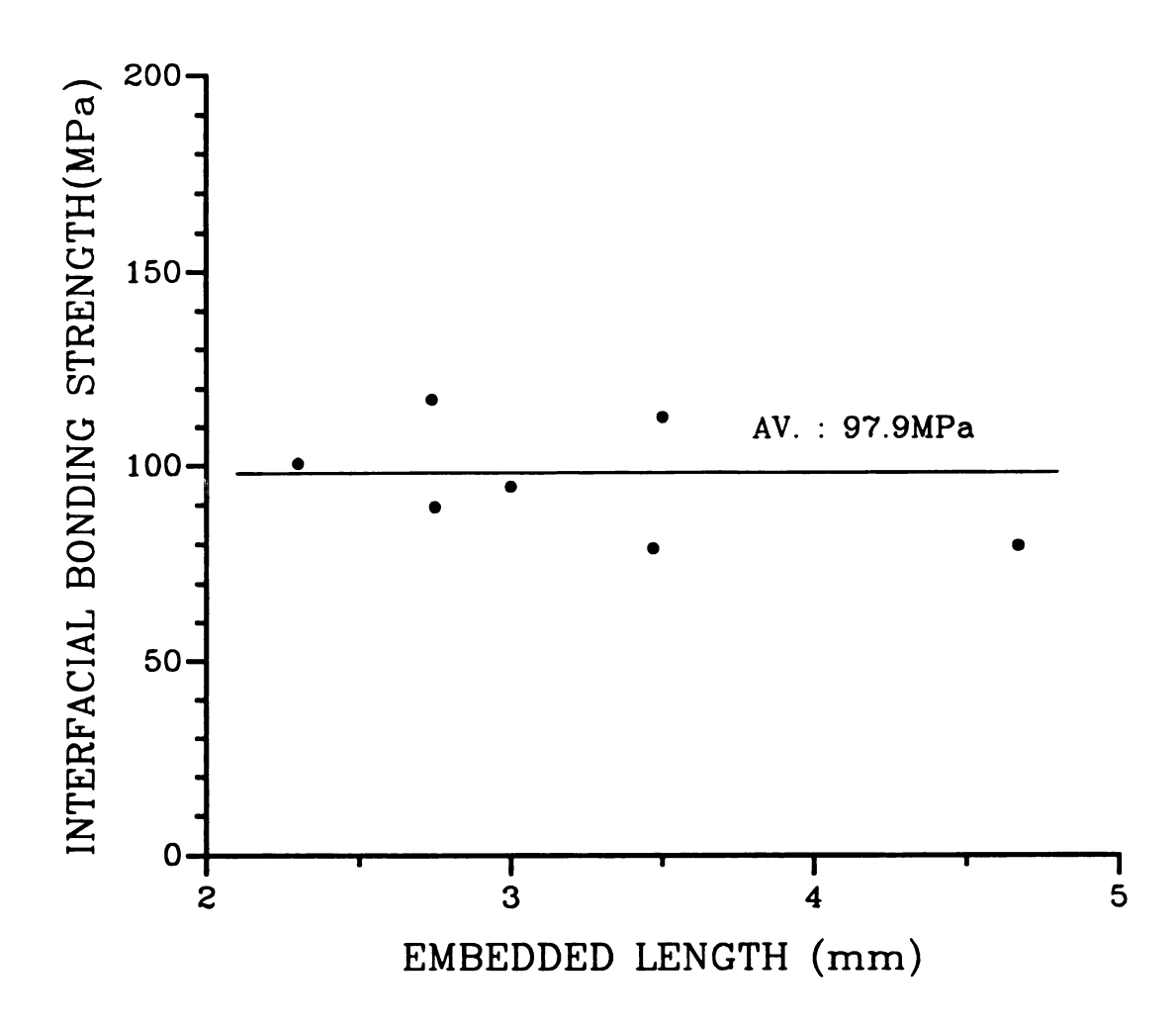


Fig.20 Interfacial shear stresses for debonding various embedded lengths of the Nichrome ribbon

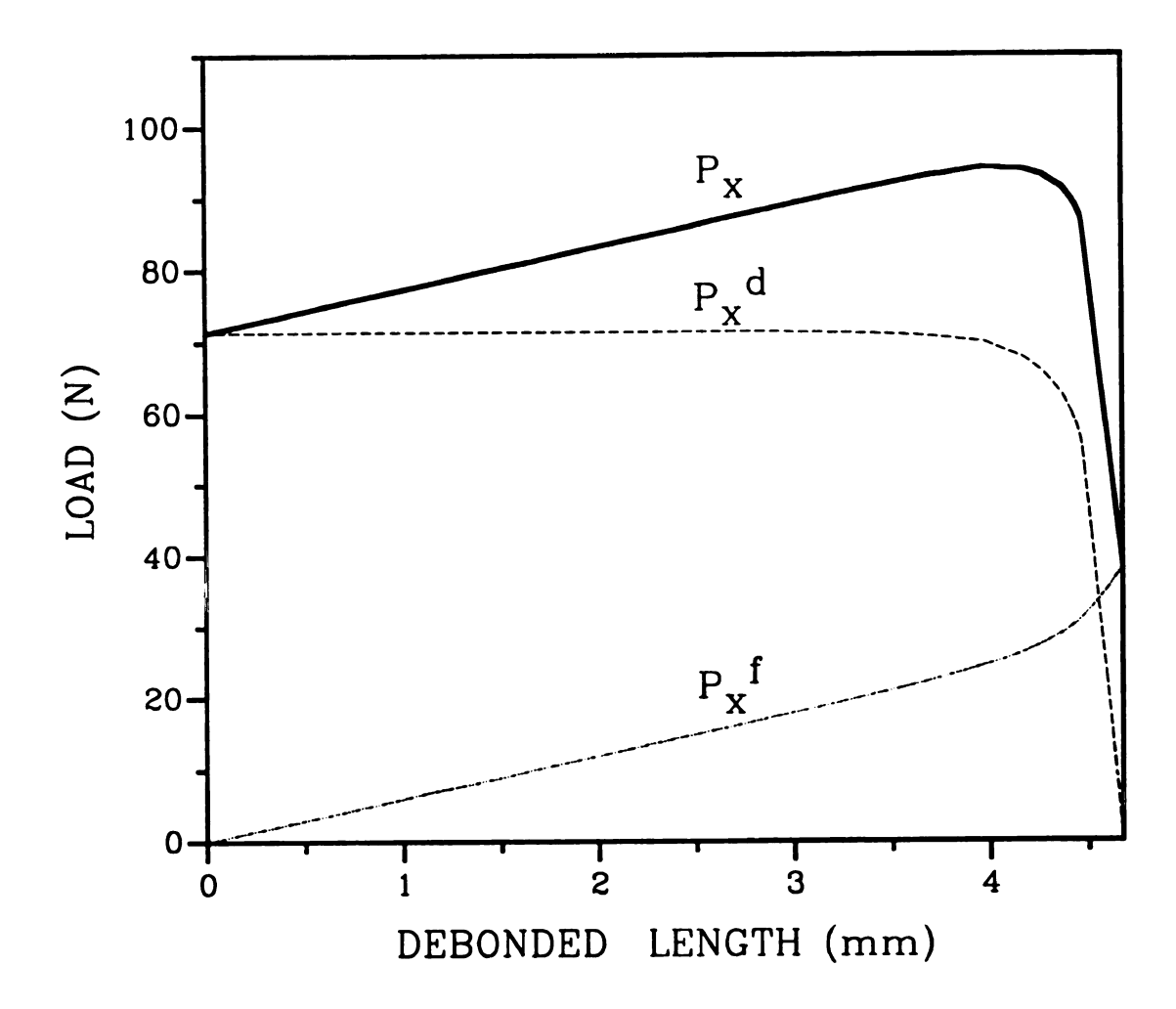


Fig.21 Loads required to continue debonding as a function of debonded length : $P_x = P_x^{\ d} + P_x^{\ f}$

length (l_e-x) at a very low rate in the beginning. However, when the bonded length(x) remains very short, P_x^{d} rapidly drops. This phenomena is attributable to the behavior of function $coth \alpha x$ in the expression for τ_x^d , and the contribution of plastic deformation of the ribbon $(\tau_{s,x}^{d})$ (Eq. 17). Especially, at short bonded length, since P_x^d is not large enough to yield the ribbon, the contribution of plastic deformation of the ribbon does not affect the plot of P_x^d . P_x^d eventually becomes zero when complete debonding is accomplished. On the other hand, the static frictional force (P_x^f) monotonically increases with debonded length $(l_e$ -x), with a rapid increase at small x due to the absence of plastic deformation of the ribbon. Since the plastic deformation of debonded ribbon is neglected in this analysis, the values of $P_{\mathbf{x}}^{f}$ obtained will be overestimations. Therefore, the sum of the above two components which represents loads required for continuation of debonding (P_x) must also be overestimated in this analysis, although the difference of maximum peak loads between this analysis (94.5N) and actual result (92.0N) was not remarkable. As shown in Fig. 21, loads required for continuation of debonding (P_x) steadily increases to a maximum and then drops. Therefore, the debonding process in this case is catastrophic at the maximum required debond load. In general, it is said that if catastrophic debonding occurs, the load suddenly drops in load-displacement curve (34). However, this sudden load drop was not observed in load-displacement curve in this experiment. It can be explained by the roughness of the debonding surfaces of the composite which influences the sliding frictional force during the pull-out of the ribbon from the matrix. The roughness of the debonded surfaces that exist in this composite (Fig. 19) may contribute to this behavior.

The effects of embedded length on the normal stress acting on the rib-

bon when debonding starts (σ_i) , and normal stress when debonding is completed (σ_f) are shown in Fig. 22. These stresses were obtained by dividing the corresponding loads by the ribbon cross-sectional area. The experimental results indicate that both σ_i and σ_f remain constant for embedded lengths in excess of a critical length. The result of σ_i agrees well with the theoretical analysis by Hseuh (35), which dealt with elastic fiber/elastic matrix system. This good agreement may be due to the fact that the term accounting for plastic deformation of ribbon (Eq. 12) is independent of the embedded ribbon length. On the other hand, contraction in thickness due to further plastic deformation of the ribbon after debonding gives clearance to debonded interface, resulting in no static frictional force. Therefore, no matter how long the embedded length may be, only certain newly debonded length undergoes static frictional force. Since σ_f is mainly affected by initial debonding stress (σ_i) and static frictional force at the debonded interface as illustrated in Fig. 21, it reaches a constant value for embedded length in excess of a critical value.

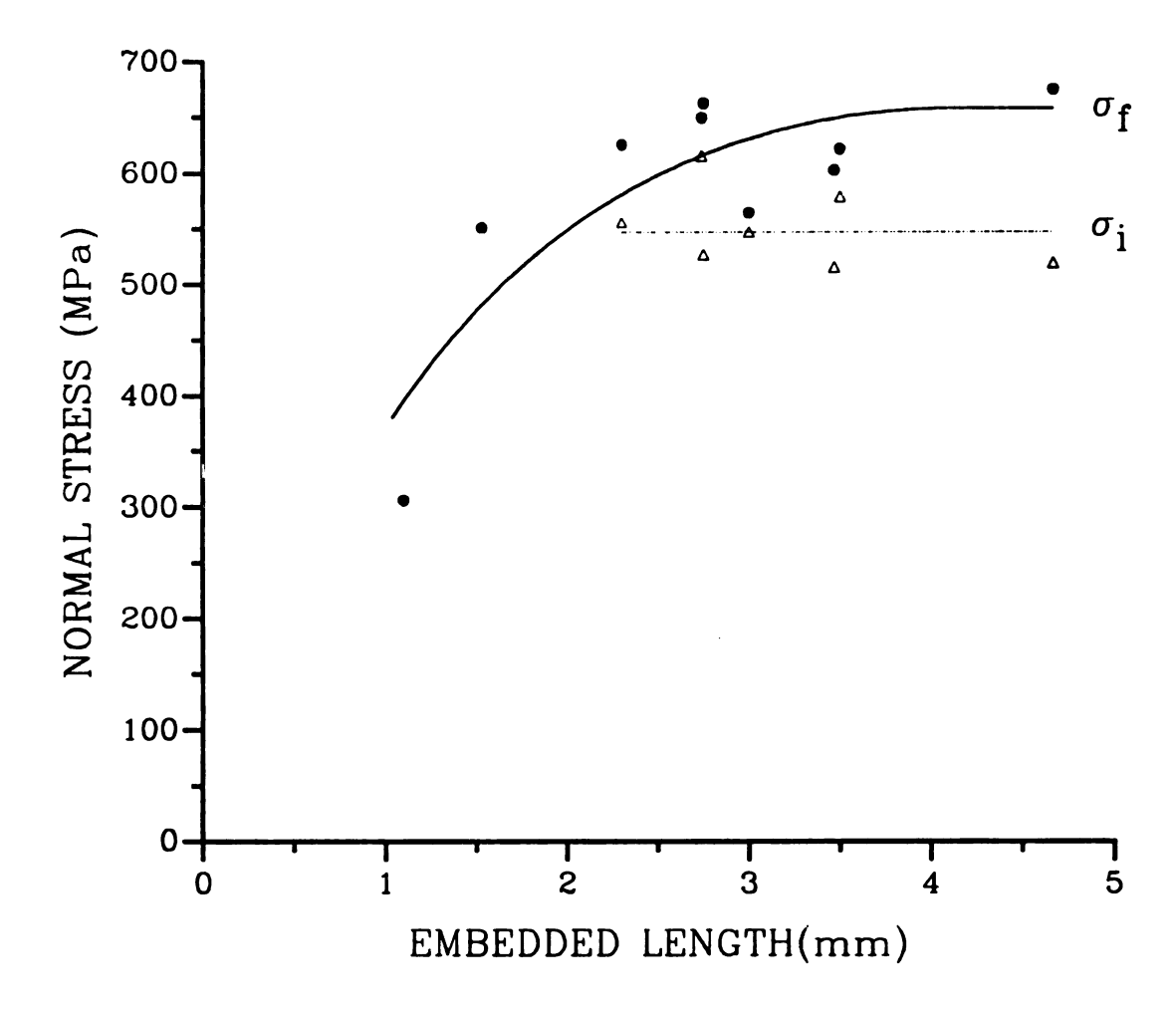


Fig.22 Effect of embedded length on the normal stress on the ribbon when debonding starts (σ_i) , and normal stress when debonding is completed (σ_f) in soda lime slide glass reinforced with Nichrome ribbon.

4-2. Interface Modifications

4-2-1. Thermal Cycling Technique

Typical stress-displacement curves of as-fabricated, and 650-TC specimens that have undergone 3, 5 and 7 cycles given in Fig. 23 illustrate that these thermal cycles significantly affect the mechanical behavior of the composite. However, stress-displacement curves of 500-TC specimens are about the same as that of the as-fabricated specimens. This behavior indicates that the thermal stresses developed in 500-TC specimens might not be high enough to cause microcracks at the interface after 5 thermal cycles. As shown in Fig. 24, in 650-TC specimens microcracks are generated at the interface after 3 thermal cycles and they link to form an almost completely connected crack after 5 thermal cycles. These SEM findings account for the observed stress-displacement behavior of the composite due to thermal cycling. In addition, a variation in stress-displacement curves for TC specimen, with various maximum cyclic temperatures, is apparent in Fig. 25. These curves were obtained after 5 thermal cycles up to each maximum cyclic temperature. Although a maximum temperature of 500°C does not cause microcracks at the interface after 5 thermal cycles, microcracks do accumulate at the interface after 5 thermal cycles with increasing maximum cyclic temperatures. The experimentally measured values of interfacial bonding strength and frictional shear stress are summarized in Tables 2 and 3.

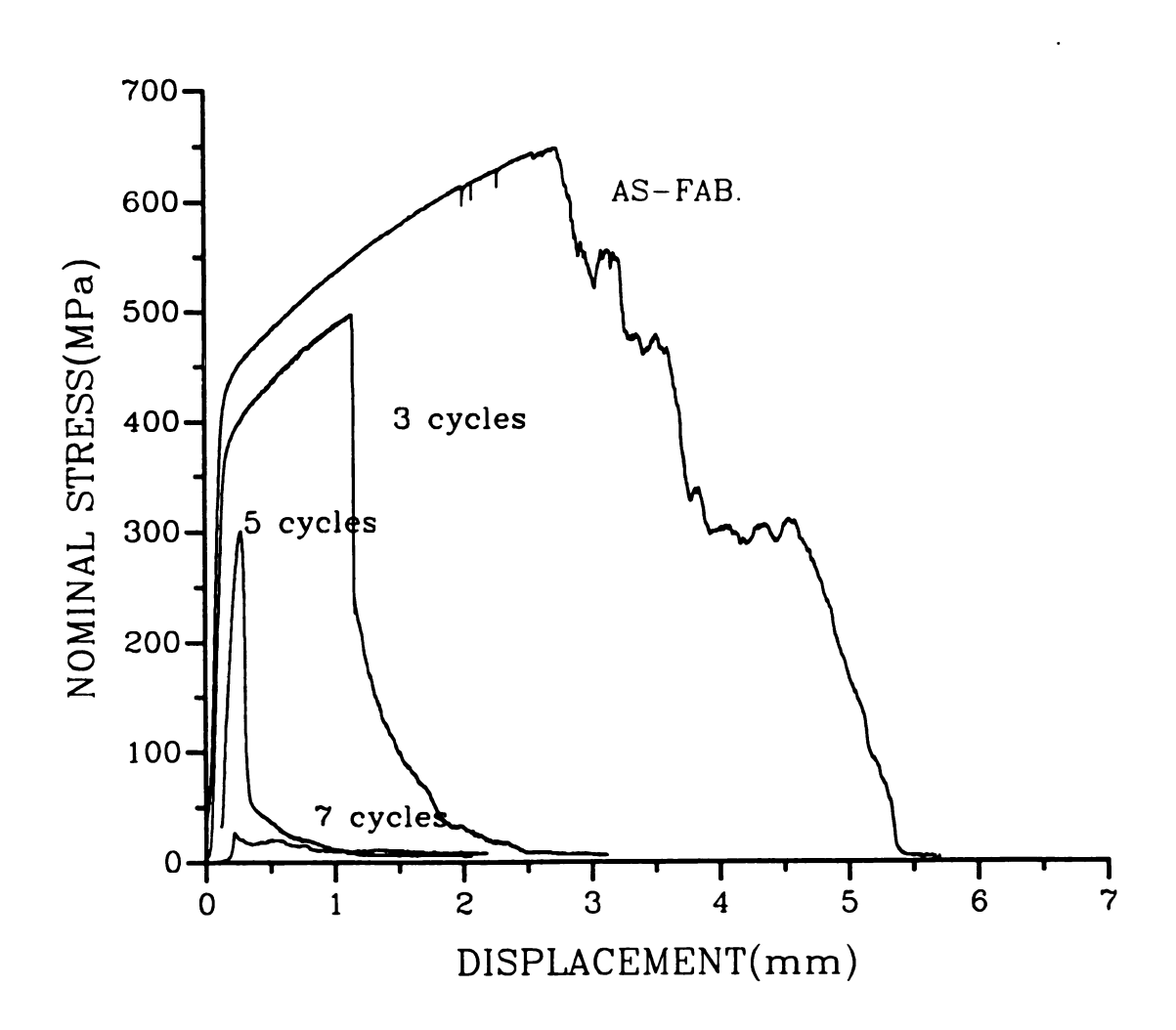


Fig.23 Typical stress-displacement curves of as-fabricated, and 650-TC specimens after various numbers of thermal cycles.

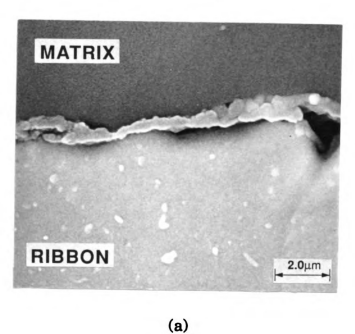
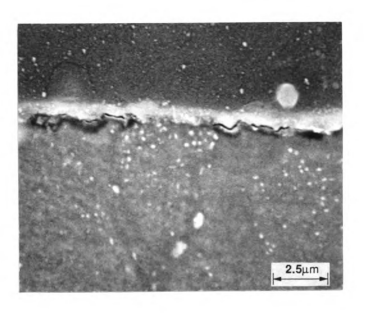
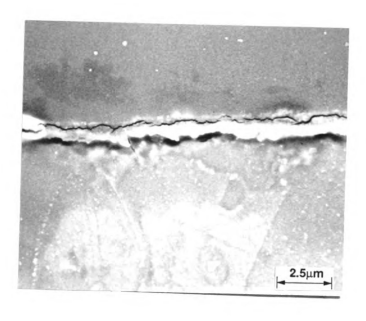


Fig.24 SEM micrographs at interfaces of (a) as-fabricated specimens, (b) 650-TC specimen after 3 cycles, and (c) 650-TC specimen after 5 cycles.



(b)

Fig.24 (continued)



(c)

Fig.24 (continued)

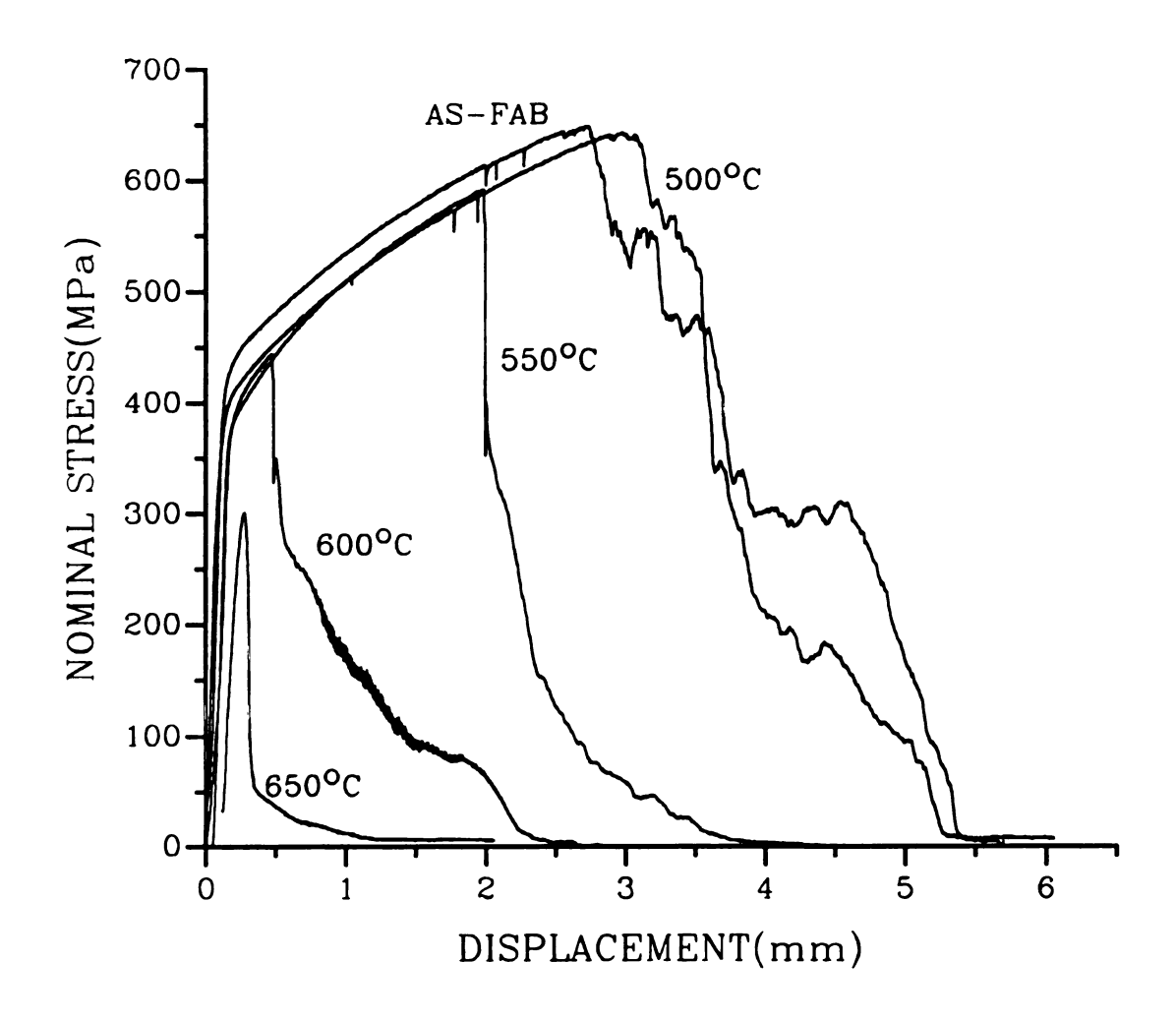


Fig.25 Stress-displacement curves of specimens that have undergone 5 thermal cycles with various maximum temperatures.

Table 2: Measured interfacial properties of 650-TC specimens after various numbers of thermal cycles

interfacial	thermal cycling conditions				
properties	i i	3 cycles	5 cycles	7 cycles	
interfacial bonding strength (MPa)	97.9 ±18.2	74.9 ±15.6	20.7 ±10.2	7.61	
frictional shear stress (MPa)	9.24 ± 2.16	3.38 ±1.13	2.62 ±1.07	1.05 ±0.44	

Table 3: Measured interfacial properties of thermal cycled specimens up to various maximum temperatures after 5 thermal cycles

interfacial	thermal cycling conditions					
properties	as-fab	500°C	550°C	600°C	650°C	
interfacial bonding strength (MPa)	97.9 ±18.2	98.1 ±7.8	83.7 ±8.4	45.2	20.7 ±10.2	
frictional shear stress (MPa)	9.24 ±2.16	10.26 ±2.48	5.05 ±2.18	4.90	2.62 ±1.07	

4-2-1-1. Effects of thermal Cycling on The Interfacial Bonding Strength and Frictional Shear Stress

The interfacial bonding strengths of 650-TC specimens that underwent various numbers of thermal cycles are given in Fig. 26. These were obtained from modified shear-lag analysis, taking plastic behavior of the metallic ribbon into account as mentioned in sec. 4-1-1 (Eqs. 14 and 15). The interfacial bonding strength decreases with increasing number of cycles and drops significantly between 3 cycles and 5 cycles. As mentioned earlier in 650-TC specimens, microcracks were generated after 3 cycles, and most of them linked together after 5 cycles, and resulted in a completely connected crack at the interface after 7 cycles. As a matter of fact, most of the specimens that have undergone 7 thermal cycles showed completely debonded interfaces. The value of the interfacial bonding strength for this condition shown in Fig. 26 was obtained from only one specimen that contained some bonded interface. The effect of maximum cyclic temperature on the interfacial bonding strength after 5 thermal cycles is presented in Fig. 27. Rapid decrease in interfacial bonding strength occurs between 500°C and 600°C.

In addition, the frictional shear stresses on the debonded surfaces of 650-TC specimens after various numbers of thermal cycles, and after 5 thermal cycles at various maximum temperatures are presented in Tables 2 and 3 respectively. These values of the frictional shear stress were calculated under the assumption that frictional shear stress is constant over the debonded region, and were obtained from dividing the initial pull-out load by total embedded area. As can be noticed from Tables 2 and 3, the fric-

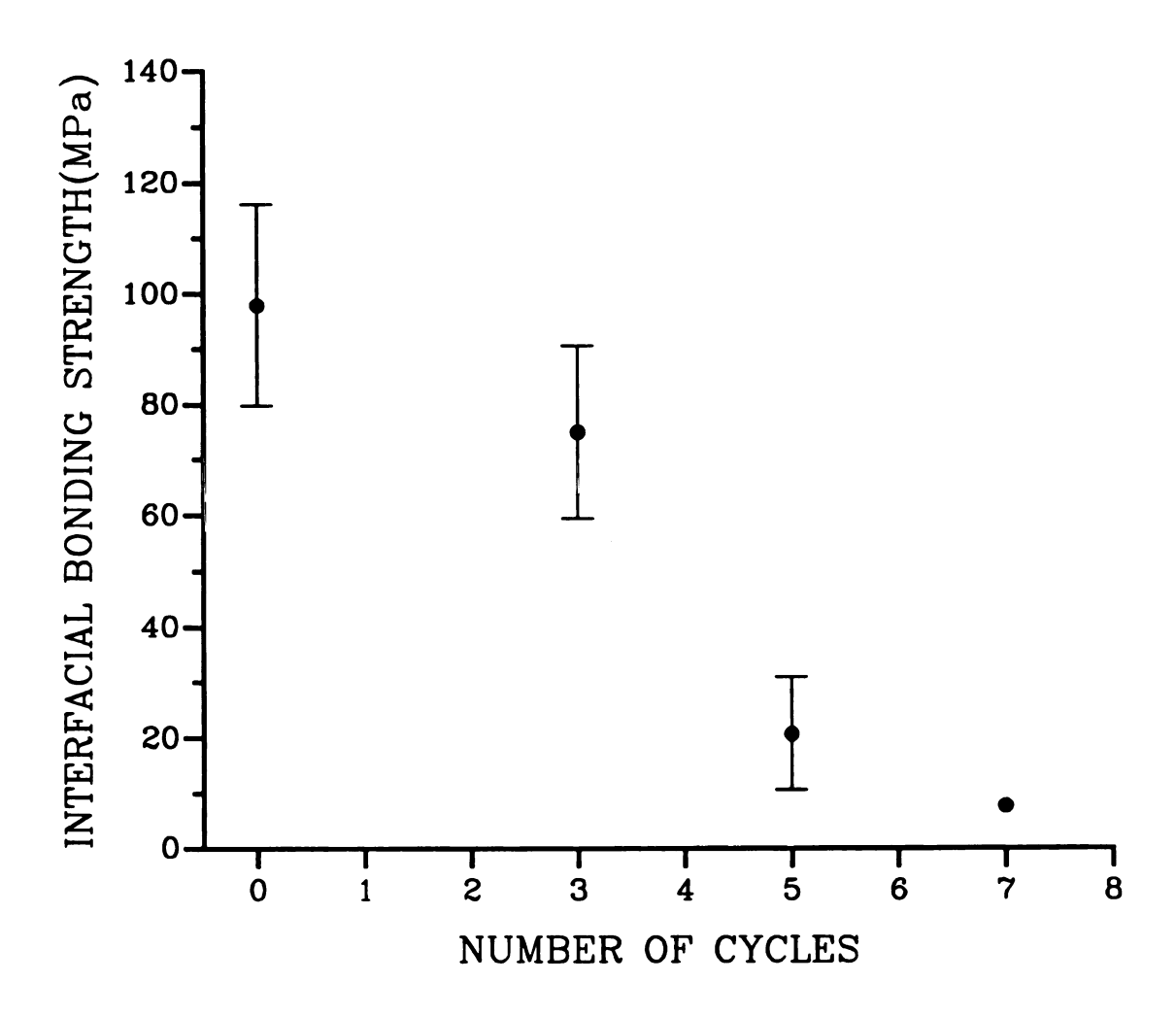


Fig. 26 Interfacial bonding strengths of 650-TC specimens after various numbers of thermal cycles.

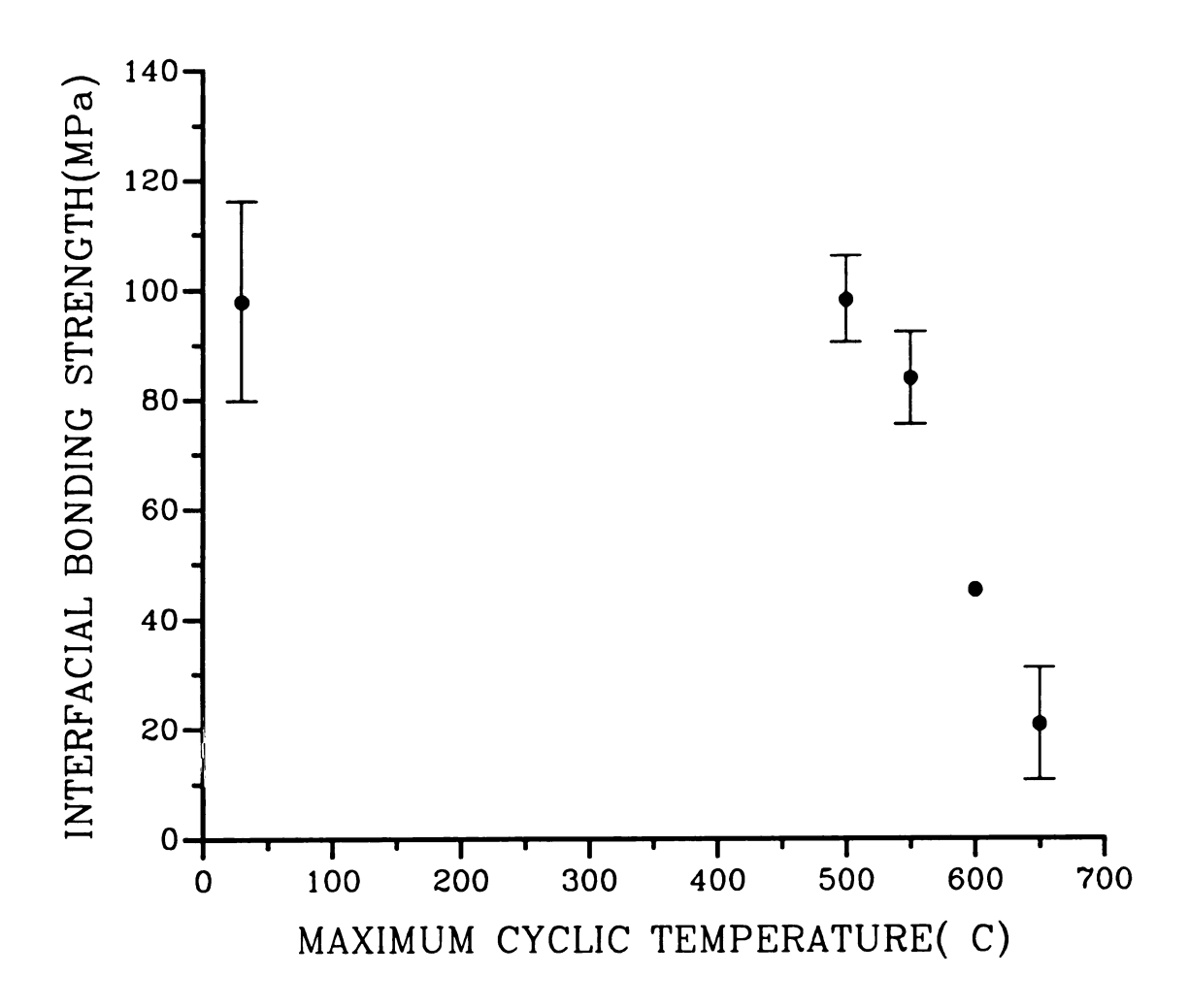


Fig. 27 The effect of maximum cyclic temperature on the interfacial bonding strength after 5 thermal cycles.

number of thermal cycles, and with increasing maximum cyclic temperature. It is believed that continual rubbing between the debonded surfaces with continued thermal cycling, or higher mismatch strain due to difference in thermal expansion coefficients with increasing maximum cyclic temperature, causes smoothening of the debonded surfaces. As a result, the frictional shear stress becomes lower due to less mechanical keying effect of debonded surfaces.

4-2-1-2. Effects of Thermal Cycling on The Complete Debonding Stress

The complete debonding stress is defined as the normal stress on the ribbon required to completely debond along the matrix-ribbon interface and is given by the maximum stress in the stress-displacement curves obtained in pull-out tests. The complete debonding stresses as a function of the embedded ribbon length in 650-TC specimens after various numbers of cycles is given in Fig. 28. The results illustrate that the complete debonding stress decreases with increasing number of thermal cycles in 650-TC specimens. After initiation of debonding, the frictional shear stress, which must be overcome to continue to debond, exists at the debonded interface due to roughness of the debonded surfaces and also due to thermal expansion mismatch between components. Therefore, the difference between the values of the complete debonding stress and the initial debonding stress, which represents the normal stress on the ribbon when debonding starts, can be considered to be such a frictional shear stress. The magnitude of frictional shear stress can be accounted for by the roughness of the debonded surfaces. As shown in Fig. 29, debonding due to thermal

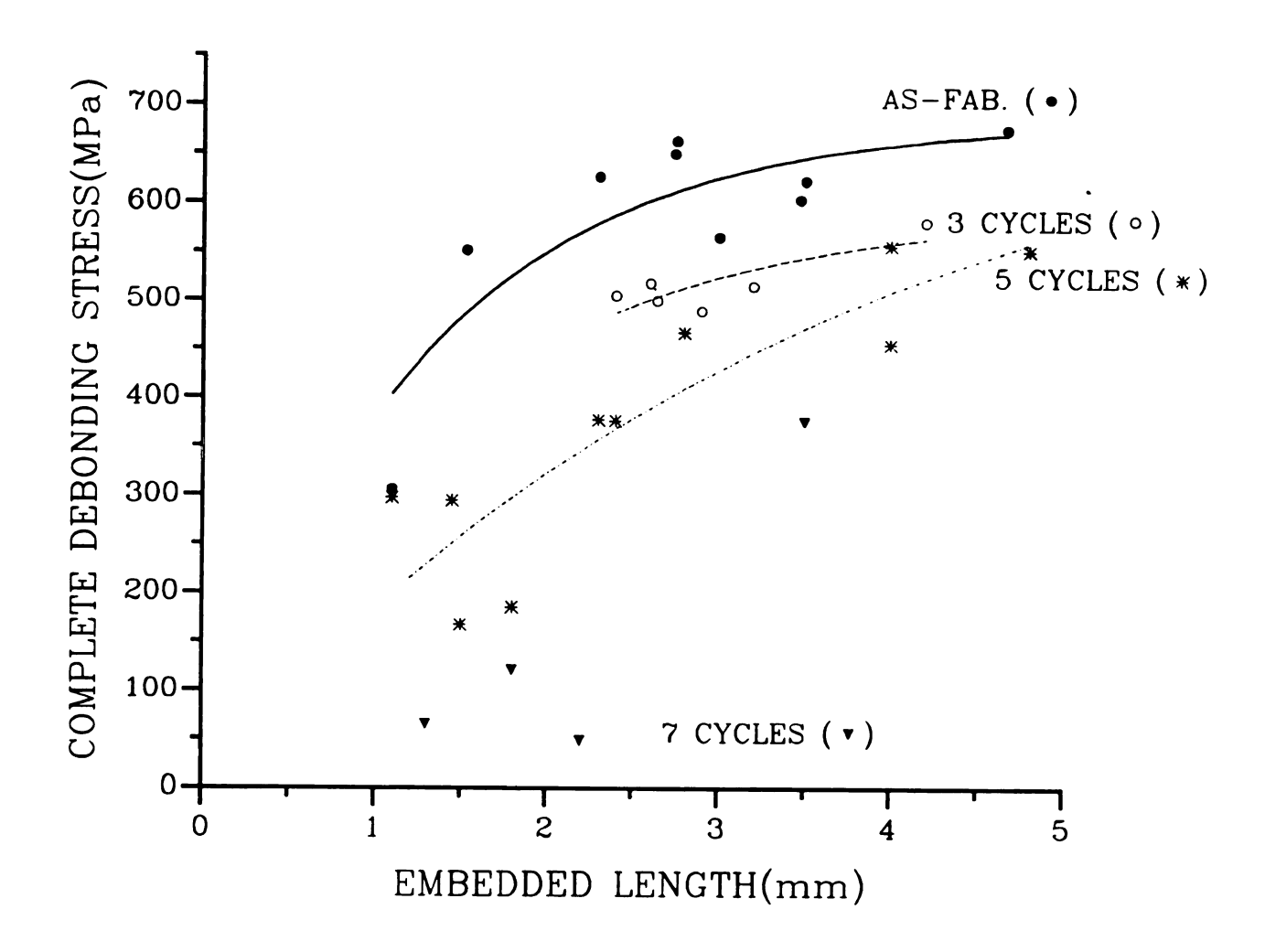
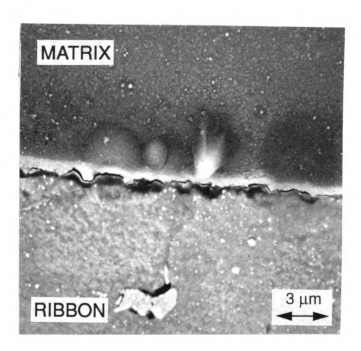
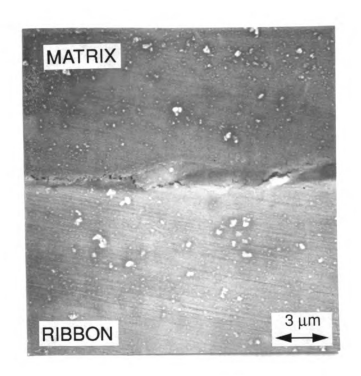


Fig. 28 The complete debonding stresses as a function of the embedded ribbon length after various numbers of thermal cycles of 650-TC specimens.



(a)

Fig. 29 SEM micrographs at debonded interface (a) due to thermal stress, and (b) due to shear stress during pull-out tests.



(b)

Fig.29 (continued)

stress generates smooth surfaces [Fig. 29(a)], while debonding due to shear stress realized in pull-out tests of embedded ribbons generate rough debonded surfaces [Fig. 29(b)]. Smoother debonded surfaces result in lower frictional shear stress, as mentioned in the previous section. In the case of as-fabricated specimens, after debonding initiates, stresses required for continuation of debonding steadily increase up to complete debonding stress due to higher frictional shear stress at the debonded interface resulting from rough interfacial cracking. However, in 650-TC specimens that have undergone 3 and 5 cycles, the frictional shear stress at the debonded interface is too low to contribute to stresses required for continuation of debonding. As a result, catastrophic debonding was observed in stress-displacement curves of these specimens. In brief, the complete debonding stress has two contributors; one is the initial debonding stress, the other is the frictional shear stress. Since both contributors decrease with increasing number of cycles, the complete debonding stress decreases with increasing number of thermal cycles. The effect of temperature on the complete debonding stress can be seen in Fig. 30. The complete debonding stresses of 650-TC specimens after 5 cycles are considerably lower, compared to those of as-fabricated ones, because both initial debonding stress and frictional shear stress decrease with increasing maximum cyclic temperature. However, 5 cycles of 500-TC do not affect the complete debonding stress or the stress-displacement curve and the interfacial bonding strength of the as-fabricated composite.

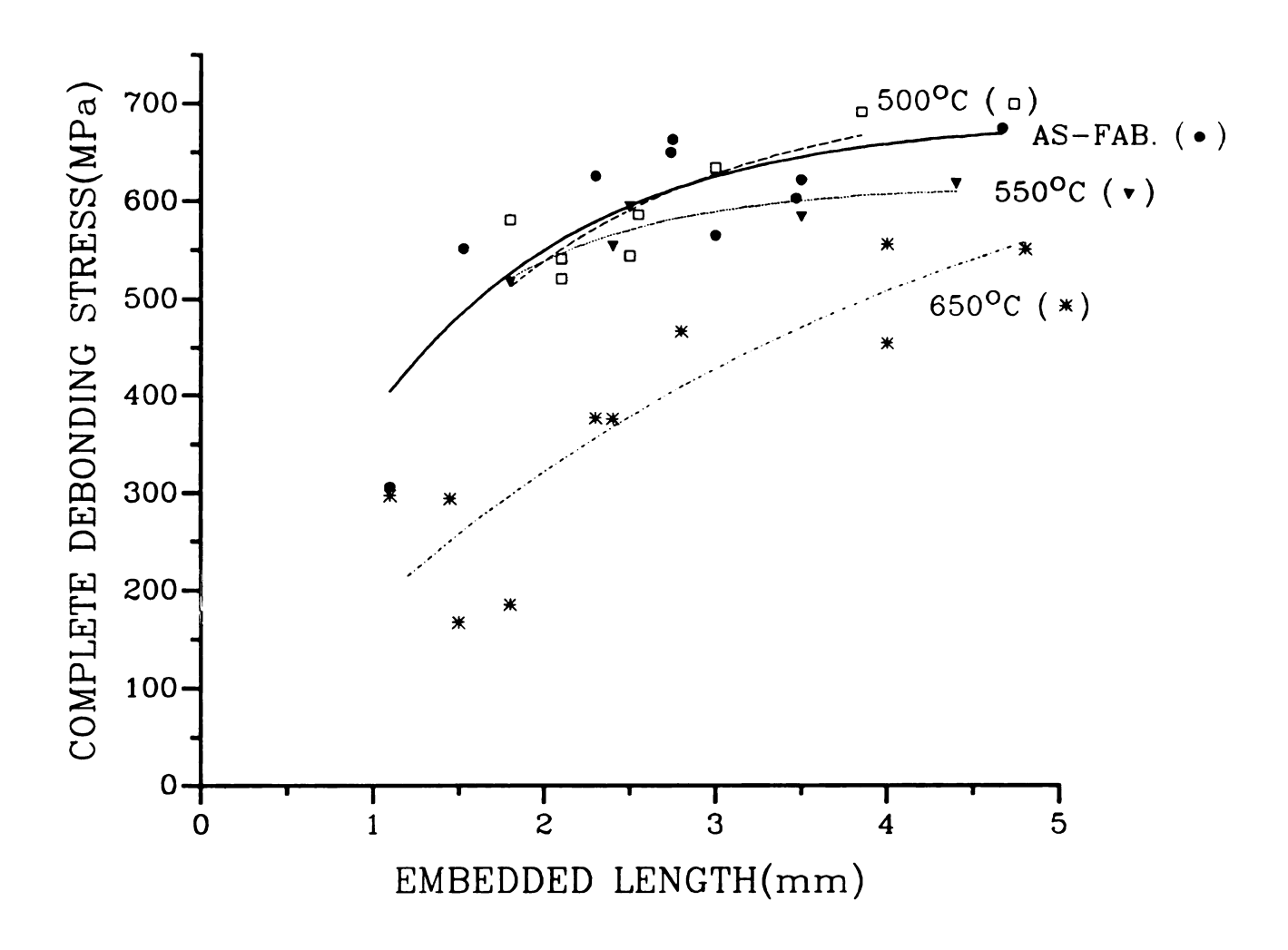


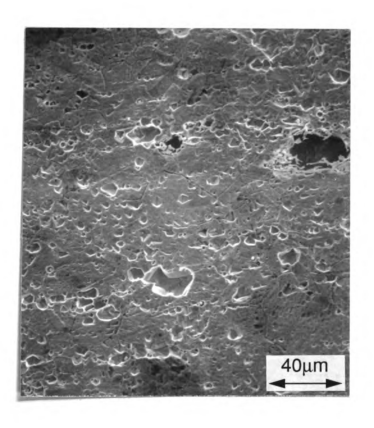
Fig. 30 The effect of maximum cyclic temperature on the complete debonding stress

4-2-2. Acid Etching of The Ribbon

The surfaces of the as-received and pre-oxidized ribbons after acid etching for a given time are shown in Fig. 31. The shapes of the dimples formed by acid etching the as-received and pre-oxidized ribbons are significantly different from each other. Since the oxide layer protects the metallic ribbon from severe attack by acid in the case of etching the pre-oxidized ribbon, the resultant density and size of dimples formed on the metallic ribbon surface were significantly reduced as compared to those in the case of etching the as-received ribbons, as can be observed later in the micrographs of metallic ribbon surfaces after ribbon pull-out.

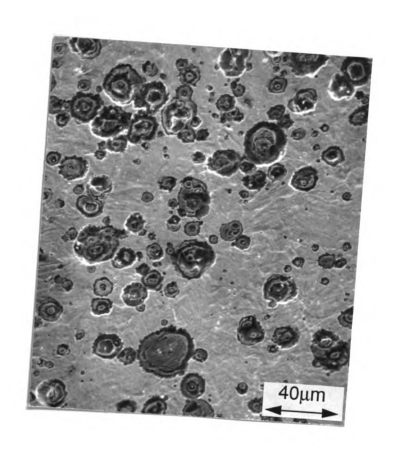
The effect of ribbon surface treatment on stress-displacement curves obtained from pull-out tests of the Nichrome ribbon embedded soda-lime glass matrix sample is illustrated in Fig. 32. The pull-out stress, defined as the normal stress on the ribbon required to initiate ribbon pull-out from the matrix, significantly changed with ribbon surface treatment. Preoxidation at 650°C for 1hr did not affect the debonding and pull-out processes in this composite. This was due to the fact that the oxide layer was also created on the as-received ribbon during composite fabrication and the debonding crack predominantly propagates along the interface between metal and oxide layer in the pull-out test as can be observed in Fig. 33. On the other hand, acid etching of the Nichrome ribbon for 60 seconds led to a large improvement in the pull-out stress of the composite. Acid etching for the same time after pre-oxidization of the ribbon at 650°C for 1 hour, however, showed only a moderate improvement in the pull-out stress.

SEM micrographs of the ribbon and the matrix surfaces after ribbon is



(a)

Fig. 31 Ribbon surfaces roughened by acid etching of (a) as-received and (b) pre-oxidized ribbons for 90 seconds



(b)

Fig. 31 (continued)

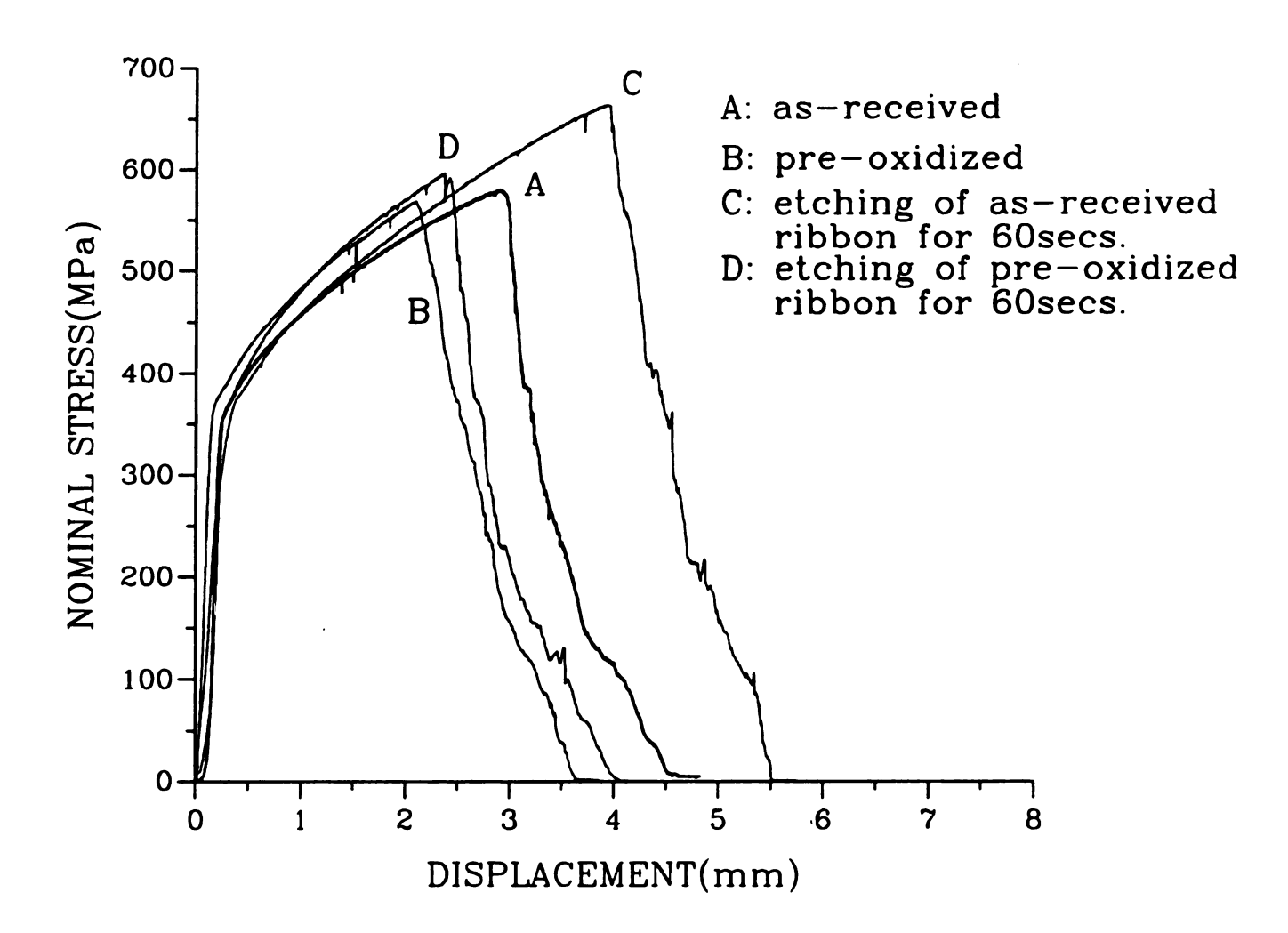


Fig. 32 The effect of ribbon surface treatment on stress-displacement curves obtained from pull-out tests.

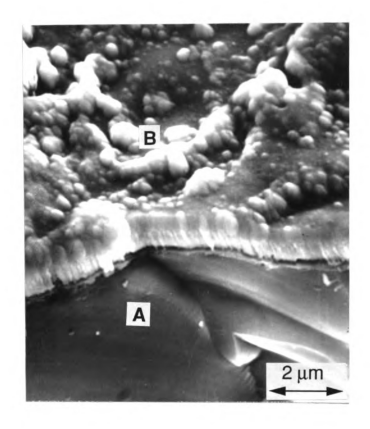
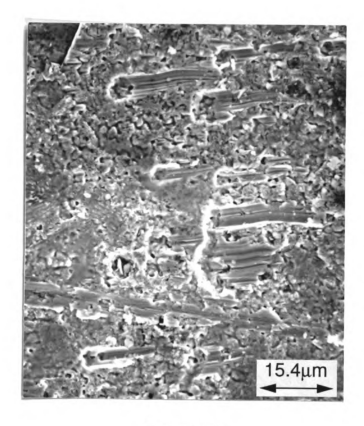


Fig. 33 Debonded surface in which debonding crack has propagated along the interface between metal and oxide layer. Oxide layer shown is stuck to the matrix after complete debonding. (A:matrix, B:oxide layer)

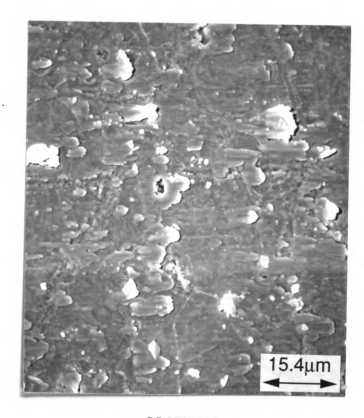
completely pulled-out from the matrix for each case of surface roughening treatment are shown in Fig. 34. The abrasion process of the jagged interface of the composite with the as-received ribbon roughened by acid etching for 60 seconds is illustrated in Fig. 34(a). In the composite with the preoxidized ribbon roughened by acid etching for 60 seconds, the portions of glass which fill the dimples on the ribbon at the jagged interface failed by shear and stuck to the ribbon during ribbon pull-out as can be seen in Fig. 34(b). Fig. 35 provides schematic illustrations of the mechanisms of ribbon pull-out processes of the composites for the different ribbon surface treatments. During composite fabrication in air, an oxide layer is formed on the ribbon surface already roughened by acid etching [Fig. 35(a)]. Dimples formed on the ribbon surface by etching, are filled up with the glass matrix. During loading, debonding crack front propagates under shear in the same manner as mentioned earlier. When debonding along the interface is complete, the ribbon is not pulled-out right away because of mechanical interlocking at the jagged interface. However, once the higher stress required to overcome the interlocking at the interface is attained, the jagged interface starts to move. This moving interface scratches the metallic ribbon surface until the interface wears out, and flattens. This mechanically interlocked interface, which exhibits features of the abrasion process of the jagged interface, results in considerable increase in the pullout stress as compared to that of the composite reinforced with the asreceived ribbon. On the other hand, for the case of pre-oxidized ribbons, after a thin oxide layer has been created on the smooth as-received ribbon surface, the ribbon is roughened by acid etching. Since the oxide layer alleviates acid attack on the metallic ribbon surface, the effect of mechanical interlocking at the jagged interface is considerably reduced under the



RIBBON

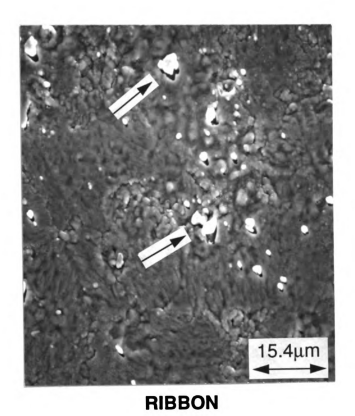
(a)

Fig. 34 SEM micrographs of the ribbon and the matrix surfaces after ribbon is completely pulled-out from the matrix for the composite with: a) the ribbon roughened by acid etching for 60 seconds, and b) the pre-oxidized ribbon roughened by acid etching for 60 seconds. Note that the abrasive process has left striations in both the matrix and ribbon in a), and portions of glass stuck to the ribbon appear as bright specks in b).



MATRIX

Fig. 34 (continued)



(b)

Fig. 34 (continued)

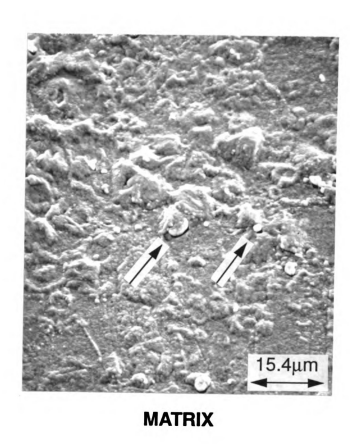


Fig. 34 (continued)

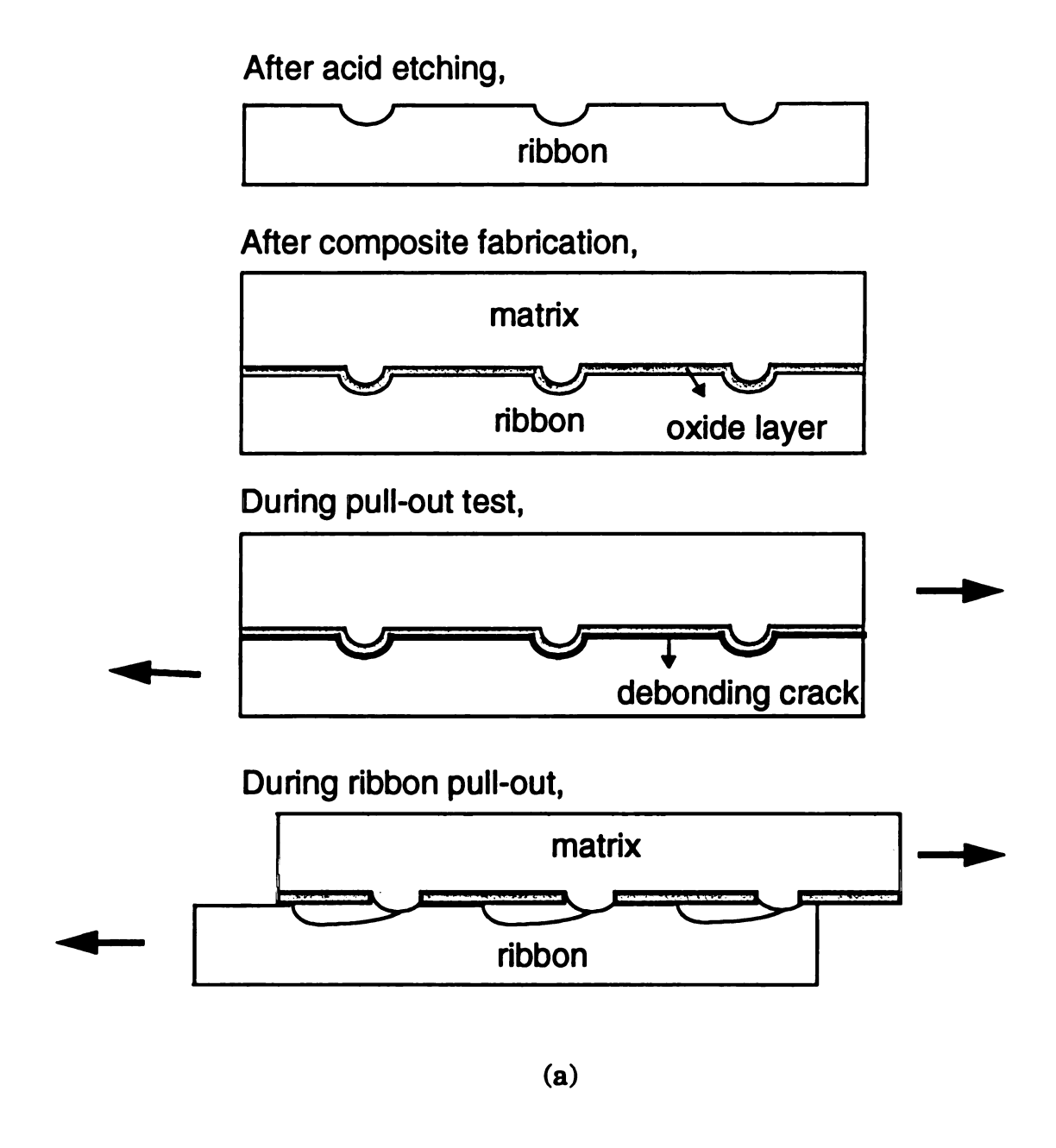


Fig. 35 Schematic profile of the interface after ribbon surface treatment, composite fabrication, and during pull-out test for the composite with: a) as-received ribbon roughened by etching, b) pre-oxidized ribbon roughened by etching. These schematics explain the mechanisms involved for processes that can cause features observed in Fig. 34.

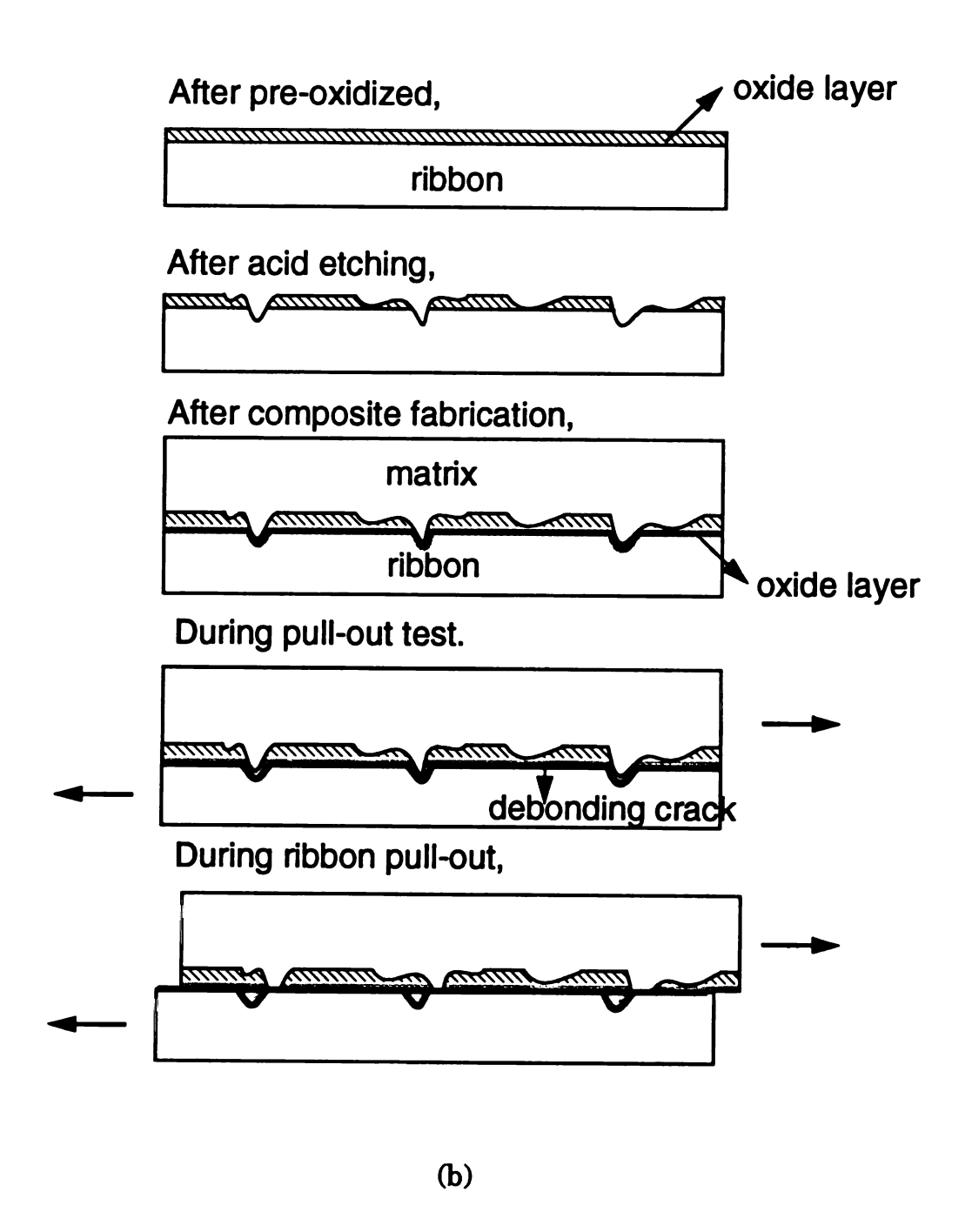
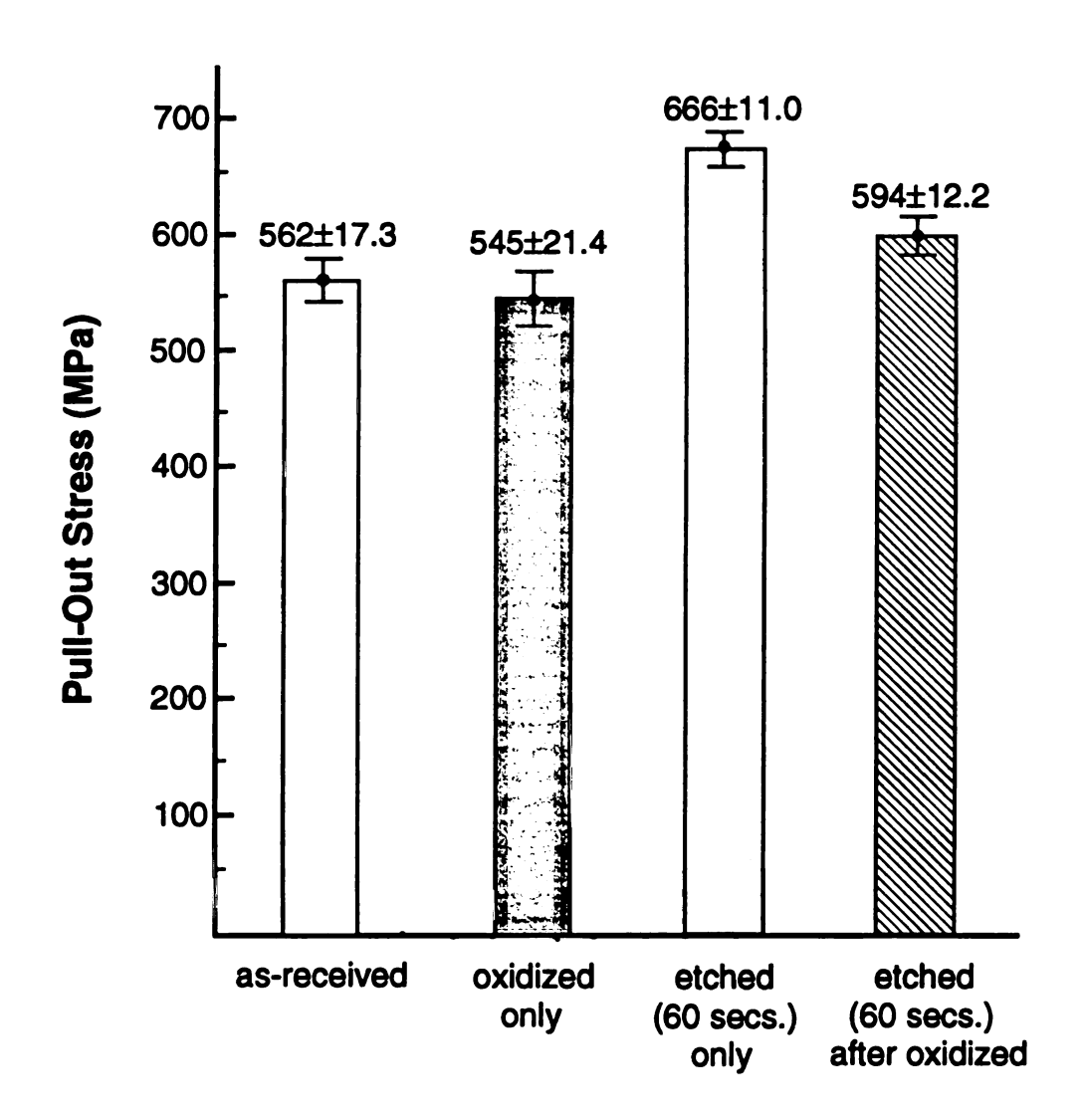


Fig. 35 (continued)

shearing action during the pull-out tests. In addition, due to the relatively low ratio of the width to the depth of jagged areas at the interface, the failure at the glass portion which fills the dimple on the ribbon surface can be expected before ribbon starts pulling-out. As a result, with this ribbon surface treatment, the pull-out stress can be obtained in a range between those of the composites reinforced with the as-received ribbon, and with the ribbon roughened by etching. Hence, this oxide layer helps in controlling more precisely the density, size and depth of the dimples, as compared to those obtainable by etching of the as-received ribbon.

Pull-out stresses of the composites containing ribbons with various surface treatments (for 1.7 mm-embedded ribbon length) are given in Fig. 36. Etching of as-received ribbon for 60 seconds resulted in 100 MPa increase in pull-out stress, as compared to that for as-received or pre-oxidized ribbons. Moreover, acid etching for 90 seconds resulted in matrix failure at the end of the embedded ribbon before ribbon starts to pull out due to high degree of interlocking at the interface. Slight increments in pull-out stresses (approximately 30 MPa) were obtained by etching the pre-oxidized ribbon for 60 seconds (as compared to as-received, and pre-oxidized ribbons).

In composites with as-received ribbon reinforcements, small load drops in stress-displacement curve representing that debonding front propagates in small jumps rather than continuously have been observed. Such a feature was not found to be significant in this study since randomly spread out jagged edges of the interface cause delayed propagation of the debonding front with etched reinforcements. This results in continuous propagation of the debonding front.



Ribbon Treatments

Fig. 36 Pull-out stress of ribbons that have undergone various treatments for an embedded length of 1.7 mm.

4-3. Fracture Toughness Behavior

4-3-1. Effect of Fracture Toughness (K_{1c}) on Interfacial Bonding

The calculated fracture toughness (K_{1c}) values of soda-lime glass matrix composites reinforced with Nichrome ribbons in various interfacial bonding conditions are given in Table 4. The interfacial bonding conditions utilized were as follows: 1) The specimens which were subjected to thermal cycling have weak interfacial bonding conditions. Moreover, it is important to note that as the number of thermal cycles increased, the interfacial bonding strength decreased. 2) The composite specimens reinforced with acid etched Nichrome ribbon showed strong interfacial bonding due to mechanical interlocking along the interface. This mechanical interlocking effect was lower in the composite with ribbons that were preoxidized prior to acid etching.

Regardless of the interfacial bonding condition, an increase of up to 20% in fracture toughness was achieved for composites with 0.5 vol% reinforcement. Prestressing of the matrix due to the thermal expansion coefficient mismatch between the matrix and ribbon and crack shielding by the ribbons may be attributed to the enhancement in fracture toughness (K_{1c}) of the present composite system. Since the thermal expansion coefficient of the ribbon is larger than that of the glass matrix, the matrix is in compression along the direction parallel to the length of the ribbon, thus providing a compressive zone which increases the level of applied stress required to open the crack (9,93,94). Crack shielding by the ribbon impedes the crack propagation and also changes crack front configuration (93,95,96). Fracto-

Table 4. Fracture toughness (K_{1c}) of soda-lime glass matrix reinforced Nichrome ribbon with various bonding conditions.

Bonding Conditions	vol%	$K_{1c}(MPa\sqrt{m})$
Matrix	0	0.98 ±0.05
NT	0.8	1.16 ±0.09
TC-3	0.5	1.22 ±0.11
TC-7	0.5	1.17 ±0.16
AE-60	0.5	1.11 ±0.04
PAE-60	0.5	1.17 ±0.09

graphic evidence of the crack shielding by the ribbon is shown in Fig. 37. The interference fringes represent the path of the crack. Fig. 37 clearly shows that the ribbon impedes the motion of the crack as it crosses the ribbon. As described by Green (95), the crack is pinned at both the edges of the ribbon, resulting in crack bowing. Following crack bowing, the secondary crack initiates behind the ribbon and propagates fast to catch up with the primary crack.

However, the interfacial debonding process which has been reported as a major mechanism of fracture toughness enhancement in fiber reinforced ceramic matrix composites was not observed during matrix cracking in the case of the present system. Catastrophic matrix failure, due to considerably low volume fraction of the ribbon in the composites, leads to negligible interfacial debonding during flexural loading.

4-3-2. Tensile Behavior of Pre-cracked Composite

Typical stress-displacement curves (with nominal stress referring to load per unit ribbon cross-sectional area) obtained from the tensile tests on the pre-cracked composite specimens with various interfacial bonding conditions are given in Fig. 38. The results given in Fig. 38 are for composites reinforced with a ribbon of 12 mm embedded length (l_e, defined in Fig. 11). In this study, the composite specimens that have undergone 3 and 7 thermal cycles between room temperature and 650°C are referred to as TC-3, and TC-7 respectively. AE-60 and AE-90 are used to refer to 60 and 90 second acid etched ribbons in as-received conditions, and PAE refers to 60 second acid etching of ribbons in preoxidized condition. NT is used for composites with ribbons in as-received condition. In the AE specimen (the

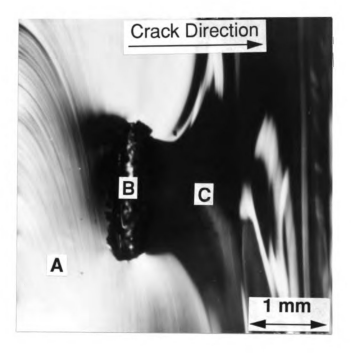


Fig. 37 Fractographic observation of the crack shielding by the ribbon. Interference fringes represent the path of the crack. Note: A: primary crack plane, B: ribbon, C: secondary crack plane. Crack direction refers to direction of crack movement.

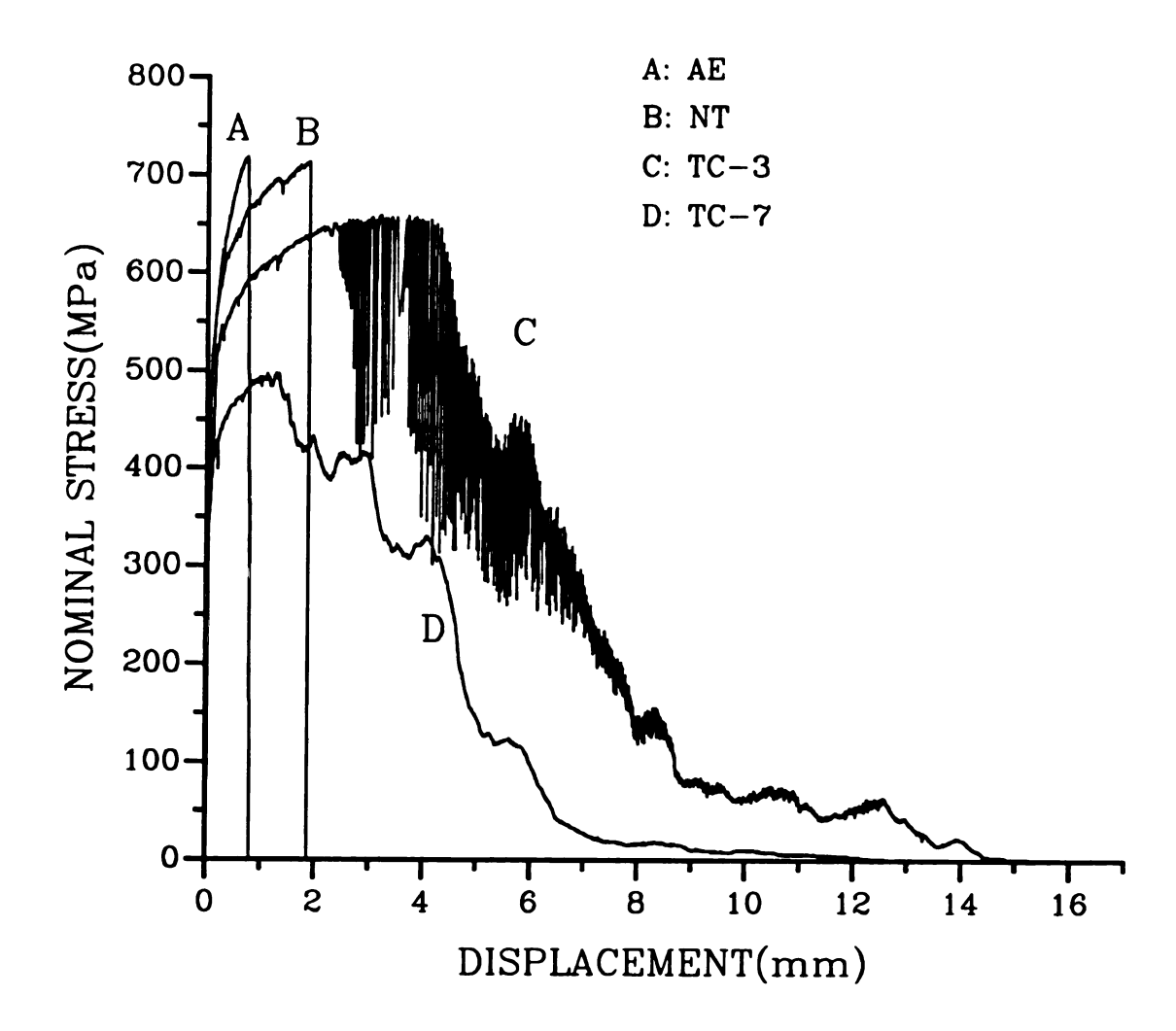


Fig. 38 Typical stress-displacement curves obtained from the tensile loading of the pre-cracked composite specimens with various interfacial bonding conditions.

.

strongest bonding condition) the ribbon fractured at a considerably small displacement (curve 'A'). As the bonding becomes weaker, the ribbon fractured at larger displacements as seen in curve 'B' for the non-treated composite specimen. The "gauge length" of the ribbon is confined to the debonded length along the embedded ribbon. Also, the debonded length decreases with an increase in interfacial bonding strength of the composite for a given applied stress. As a result, a general trend, in spite of some inconsistencies, indicating that the displacement at the point where the ribbon fractured decreased with an increase in the interfacial bonding strength can be noted in the data provided in Table 5. On the other hand, the ribbon pull-out from the matrix after complete debonding was observed in TC-3 and TC-7 specimens (curves 'C' and 'D', respectively). However, there was noticeable difference between these two cases. For TC-3 specimens, the interfacial bonding was strong enough to prevent complete debonding of the ribbon during initial stages of the test. As a result, the effective length of the bonded portion of the ribbon was large enough to sustain considerable plastic deformation, before complete debonding occurred. On the other hand, in the TC-7 specimens containing mostly inter-connected microcracks, the interfacial bonding was so weak that the debonding crack propagated more easily along the interface as compared to the TC-3 specimen. In addition to this, the low static frictional shear stress at the debonded interface (in TC-7) was not effective enough to hold the debonded portion of the ribbon. Therefore, complete debonding occurred at a much lower stress than that of the TC-3 specimen. Hence, the extent of plastic deformation was very low in the case of the TC-7 specimens. However, the displacement at a given stress level was considerably large when compared to that of the TC-3 specimen because of the differ-

Table 5. Effect of interfacial bonding on the displacement at the ribbon fracture.

Bonding Condition	AE- 60	PAE- 60	AE- 60	NT	TC-3	TC-7
Displacement at Ribbon Fracture (mm)	0.67 0.05	0.85 0.28	1.02	1.64 0.50	1.63 0.58	1.48 0.24

ence in the debonded length ("gauge length") of the ribbon between both cases.

The heavy shaded portion observed in the case of TC-3 specimen (Fig. 38) indicates the "stick-slip" friction phenomenon. In this portion of the curve, each load drop was accompanied by an audible "click". The mechanism of this phenomenon has been explained by Griffin et al. (50) and Deshmukh et al. (49). According to Griffin et al., the Poisson contraction and expansion of the fiber in combination with a difference between static and dynamic friction leads to stick-slip friction. In contrast, Deshmukh et al. pointed out that the release of excess strain energy stored in the free length of the fiber when the fiber reloads contributes to the above phenomenon. As illustrated in curve 'C', the stress amplitude and wavelength of the stick-slip behavior decreases as the ribbon is progressively pulled out. This can be explained by the smoothening effect of the debonded interface during ribbon pull-out, since such a behavior predominantly depends on the asperities of the debonded surfaces at the interface. The stick-slip behavior was not observed in the TC-7 specimens due to the smooth feature of the debonded interface, resulting in low frictional shear stress.

4-3-3. Toughness due to Crack Bridging (ΔG_c)

Fracture toughness due to crack bridging (ΔG_c) in the composite under various bonding conditions was evaluated using Eq. 8 and the area under the stress-displacement curves. The results are given in Table 6. Enhancement in fracture toughness resulting from thermal cycling (curve 'C') of the composite [as compared to that of as-received ribbon (curve 'B'), or acid-etched ribbon (curve 'A')] can be observed in Fig. 38. Plastic defor-

Table 6. Fracture toughness due to crack bridging (ΔG_c) in various bonding conditions. $\Delta G_c = V_f \, x \, \text{area under the stress-displacement curve in Fig. 38}.$

	$\Delta G_{c} (KJ/m^{2})$					
	Plastic deformation	Frictional sliding	Total			
NT	6.08	0	6.08			
AE-60	2.87	0	2.87			
TC-3	7.03	13.48	20.51			
TC-7	3.25	7.67	10.92			

mation and frictional sliding play important roles in the enhancement of fracture toughness due to thermal cycling (curve 'C'). For as-received or acid-etched ribbons, the lower fracture toughness realized can be attributed to the ribbon fracture prior to the onset of any extensive plastic deformation. It is evident from curves 'A' and 'B' that stronger the interfacial bonding the smaller is the area under the curve, due to the small displacement at ribbon fracture. Even though both the curves 'C' and 'D' are comprised of plastic deformation and frictional sliding stages, the total area under curve 'D' is much smaller than that of the curve 'C', because of the low plastic deformation and low frictional shear stress involved in curve 'D'. From these observations, it can be inferred that TC-3 specimen with 11mm-embedded length of the ribbon shows the maximum fracture toughness due to crack bridging (ΔG_c). In addition, the effect of the embedded ribbon length on toughness of non-treated composite specimens is shown in Fig. 39. The ribbon fractured in the composite with over 12mm-embedded ribbon length, while ribbon pull-out occurred after plastic deformation of the debonded ribbon in the composite with less than 11mm-embedded ribbon length. As a result, the maximum fracture toughness due to crack bridging (ΔG_c) in the non-treated composite was achieved at 11mm-embedded ribbon length. Therefore, it can be defined as "critical embedded length (l_{cr}) " for the maximum fracture toughness due to crack bridging in a given bonding condition (and for the given ribbon thickness) since the ribbon with this length effectively undergoes both plastic deformation and frictional sliding phenomena. The critical embedded length in various bonding conditions is shown in Table 7. Due to the wide variation in data, the results were presented as a range, instead of a single value. Nevertheless, it can be concluded from the results of this study that the maximum

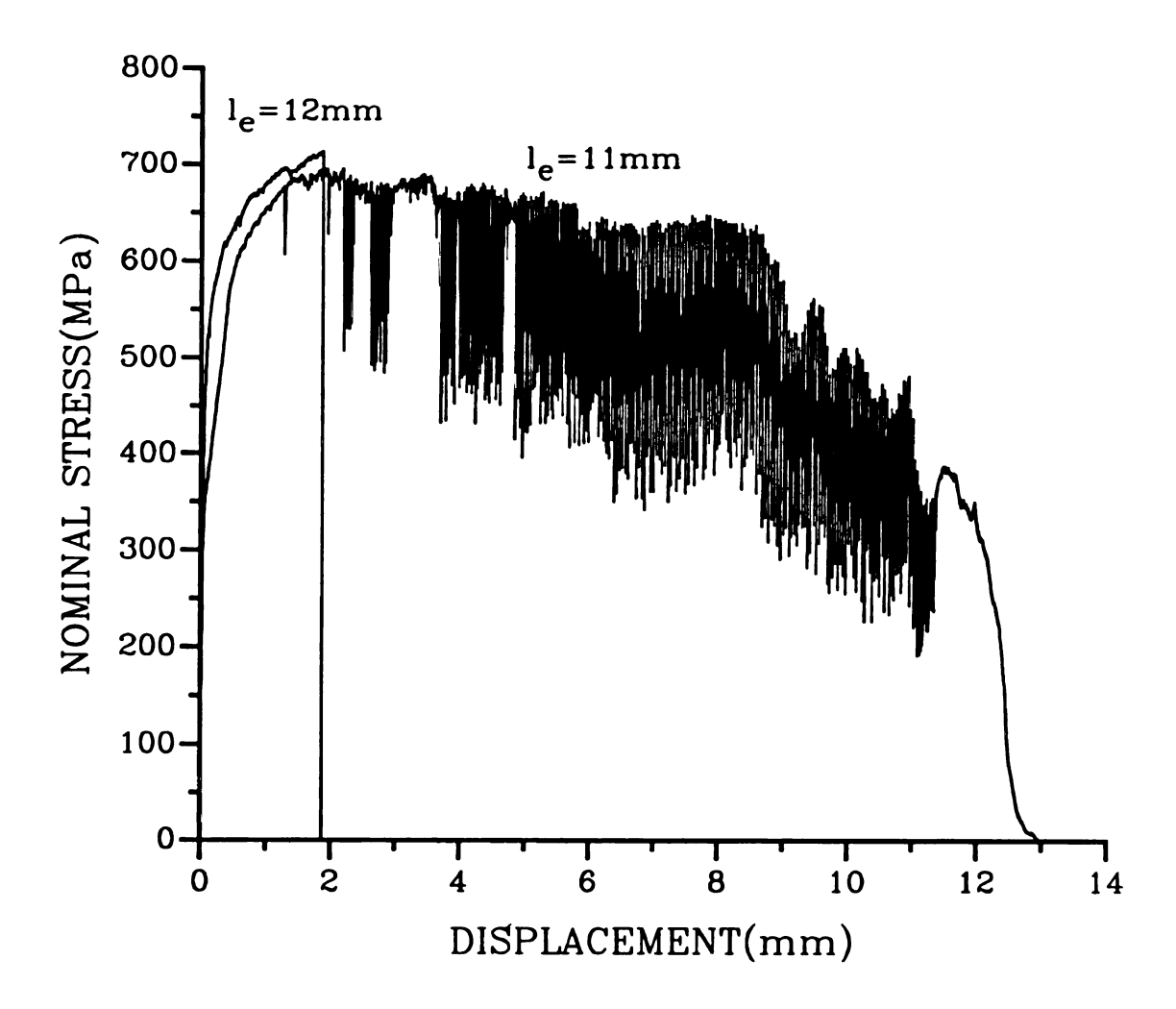


Fig. 39 Stress-displacement curves showing the effect of the embedded ribbon length on toughness (ΔG_c) of NT composite specimens.

Table 7. Critical embedded length $(l_{\rm e})$ for the maximum fracture toughness due to crack bridging in various bonding conditions.

Bonding Conditions	NT	AE-60	PAE-60	TC-3	TC-7
Critical Embedded Length (mm)	10~12	less than 3	less than 3	10~13	15~17

fracture toughness due to crack bridging can be achieved by using discontinuous metallic reinforcements with a length less than or equal to the critical embedded length in the ceramic matrix composites.

5. Conclusions

Metallic ribbons embedded in a ceramic matrix may debond from the matrix due to the combined effects of plastic behavior of the metallic ribbon and the distribution of shear stress along the embedded ribbon (shear lag model). Hence, the plastic behavior of the metallic ribbon was taken into account in analyses of ribbon pull-out in present study. The interfaces between Nichrome ribbon and soda lime glass matrix were modified by means of various numbers of thermal cycles, and various maximum temperatures used in thermal cycles. The interfacial bonding strength, complete debonding stress and frictional shear stress were measured by pull-out tests on thermally cycled specimens. Also, the interface of this composite was modified by acid etching of as-received or oxidized ribbon surface. Finally, on the basis of above interface modifications, interfacial effects on mechanical properties of brittle matrix with ductile reinforcement were evaluated. The important observations are summarized below:

- 1) Plastic deformation of ductile ribbon provides significant contribution to the resultant interfacial shear stress (τ_t) at the interface in ductile ribbon reinforced brittle matrix composites.
- 2) Although the debonding process in this composite is catastrophic at the maximum required debond load, mechanical keying due to the roughness of the debonded surfaces may prevent a sudden load drop.
- 3) The applied tensile stresses required to initiate and complete debonding

 $(\sigma_i$ and σ_f respectively) are independent of the embedded length in excess of a critical value.

- 4) Microcracks at the interface of 650-TC specimens are generated after 3 thermal cycles, they link together after 5 cycles, and make a completely connected crack after 7 cycles. A 500-TC treatment might not create enough thermal stresses to generate microcracking at the interface after 5 cycles.
- 6) The interfacial bonding strength decreases with increasing number of thermal cycles and drops significantly after 5 cycles of 650-TC.
- 7) Frictional shear stress on the debonded surfaces decreases with increasing number of thermal cycles due to smoothening effect which results from continual rubbing between the debonded surfaces during continued thermal cycling.
- 8) The complete debonding stress decreases with increasing number of thermal cycles because both contributors, initial debonding stress and frictional shear stress, decrease with increasing number of cycles.
- 9) The results of this study suggest that optimum interfacial bonding strength of soda-lime glass/Nichrome ribbon composite can be achieved by thermal cycling.
- 10) Acid etching of the ribbon gives rise to considerable improvement in pull-out stress of the composite. However, it is very difficult to control the

pull-out stress because ribbon is severely attacked by the acid even in very short time period.

- 11) A pre-oxidation treatment of the ribbon surface before etching can protect the metallic ribbon from severe attack by acid so as to provide a better control of the ribbon pull-out behavior in the composite.
- 12) In composites with etched ribbons, randomly spread-out jagged interface causes delayed propagation of debonding front, and consequently debonding front propagates continuously rather than in small jumps, a feature exhibited by the composites reinforced with smooth ribbons.
- 13) Increases of fracture toughness (K_{1c}) of these composites up to 20% were achieved due to "prestressing of the matrix" and "crack shielding by the ribbon".
- 14) Introduction of even a very low volume fraction of metallic ribbon provides significant improvement in fracture toughness due to crack bridging (ΔG_c) of the brittle glass matrix.
- 15) To obtain maximum toughness in this composite, it is essential to retain the optimum bonding strength.
- 16) The results of this study suggest that enhancement in toughness may be achieved by using discontinuous metallic ribbon reinforcement in the brittle ceramic matrix ($l_e \le l_{cr}$).

References

- 1) D.C. Phillips, J. Mater. Sci., 9 (1974) 1847
- 2) K.M. Prewo and J.J. Brennen, J. Mater. Sci., 15 (1980) 463
- 3) J. Brennen and K. Prewo, J. Mater. Sci., 17 (1982) 2371
- 4) K.M. Prewo and J.J. Brennen, J. Mater. Sci., 17 (1982) 1201
- 5) A.G. Evans and R.M. McMeeking, Acta metall., 34 (1986) 2435
- 6) M.D. Thouless and A.G. Evans, Acta metall., 36 (1988) 517
- 7) L.S. Sigl and H.F. Fischmeister, Acta metall., 36 (1988) 887
- 8) B. Budiansky, J.C. Amazigo and A.G. Evans, J. Mech. Phys. Solids, 36 (1988) 167
- 9) A.G.Evans and D.B. Marshall, Acta metall., 37 (1989) 2567
- 10) A.G. Evans, Mater. Sci. Eng., A107 (1989) 227
- 11) L.S. Sigl and A.G. Evans, Mech. Mater., 8 (1989) 1
- 12) E. Bischoff, O. Sbaizero, M. Rühle, and A.G. Evans, J. Am. Ceram. Soc.,72 (1989) 741
- 13) A.G. Evans, J. Am. Ceram. Soc., 73 (1990) 187
- 14) S.V. Nair, J. Am. Ceram. Soc., 73 (1990) 2839
- 15) G.H. Campbell, B.J. Dalgleish, M. Rühle and A.G. Evans, J. Am. Ceram. Soc., 73 (1990) 521
- 16) G.A. Cooper and A. Kelly, J. Mech. Phys. Solids, 15 (1967) 279
- 17) P. Hing and G.W. Groves, J. Mater. Sci., 7 (1972) 427
- 18) V.D. Krstic, P.S. Nicholson and R.G. Hoagland, J. Am. Ceram. Soc., 64 (1981) 499
- 19) V.D. Krstic, Philos. Mag. A48 (1983) 695

- 20) M.S. Newkirk, A.W. Urqhart and H.R. Zwicker, J. Mater. Res. 1 (1986) 81
- 21) L.S. Sigl, P.A. Mataga, B.J. Dalgeish, R.M. McMeeking and A.G. Evans, Acta metall., 36 (1988) 945
- 22) M.F. Ashby, F.J. Blunt and M. Bannister, Acta metall., 37 (1989) 1847
- 23) H.C. Cao, B.J. Dalgleish, H.E. Dève, C.K. Elliot, A.G. Evans, R. Mehrabian and G.R. Odette, Acta metall., 37 (1989) 2969
- 24) B. Flinn, M. Rühle and A.G. Evans, Acta metall., 37 (1989) 2969
- 25) H.E. Dève, A.G. Evans, G.R. Odette, R. Mehrabian, M.L. Emiliani and R.J. Hecht., Acta metall. mater., 38 (1990) 1491
- 26) G. Baran, M. Degrange, C.Roques-Carmes and D. Wehbi, J. Mater. Sci., 25 (1990) 4211
- 27) K.S. Ravichadran, Acta metall. mater., 40 (1992) 1009
- 28) F.E. Heredia, M.Y. He, G. E. Lucas, A.G. Evans, H.E. Dève and D. Konitzer, Acta metall. mater., 41 (1993) 505
- 29) L.B. Greszczuk, in "Interfaces in Composites", ASTM STP 452 (American Society for Testing and Materials, 1969) p. 42.
- 30) P. Lawrence, J. Mater. Sci. 7 (1972) 1.
- 31) A. Takaku and R.G.C. Arridge, J. Phys. D: Appl. Phys. 6 (1973) 2038.
- 32) P. Bartos, J. Mater. Sci. 15 (1980) 3122.
- 33) C.W. Griffin, S.Y. Limaye, D.W. Richerson and D.K. Shetty, Ceram. Eng. Sci. Proc. 9 (1988) 671.
- 34) R.W. Goettler and K.T. Faber, Ceram. Eng. Sci. Proc. 9 (1988) 861.
- 35) Chun-Hway Hsueh, Mater. Sci. and Eng. A123 (1990) 1.
- 36) V.M. Karbhari and D.J. Wilkins, Scrip. Metall. Mater. 24 (1990) 1197.
- 37) R.W. Rice, J.R. Spann, D. Lewis and W. Coblenz, Ceram. Eng. Sci. Proc., 5 (1984) 614

- 38) B. Bender, D. Shadwell, C Bulik, L. Invorvati and D. Lewisill, Am. Ceram. Soc. Bull., 65 (1986) 363
- 39) R.A. Lowden and D.P. Stinton, Ceram. Eng. Sci. Proc., 9 (1988) 705
- 40) R.N. Singh, Ceram. Eng. Sci. Proc., 10 (1989) 883
- 41) L.P.Zawada and R.C.Wetherhold, J. Mater. Sci., 26 (1991) 648
- 42) R.H. Moore and S.C. Kunz, Ceram. Eng. Sci. Proc., 8 (1987) 839
- 43) M.J. Klein, in "Composite Materials", 1: Interfaces in Metal Matrix Composites, edited by A.G. Metcalf, L.J. Broutman and R.H. Krock (Academic, New York, 1974) 169
- 44) D.H. Grande, J.F. Mandell and K.C.C. Hong, J. Mater. Sci. 23 (1988) 311
- 45) A. Kelly and W.R. Tyson, J. Mech. Phys. Solids, 13 (1965) 329
- 46) V. Laws, Composites, 13 (1982) 145
- 47) R.J. Gray, J. Mater. Sci., 19 (1984) 861
- 48) M.R. Piggott, Comp. Sci. Tech., 30 (1987) 295
- 49) U.V. Deshmukh and T.W. Coyle, Ceram. Eng. Sci. Proc., 9 (1988) 627
- 50) C.W. Griffin, S.Y. Limaye, D.W. Richerson and D.K. Shetty, Ceram. Eng. Sci. Proc., 9 (1988) 671
- 51) Chun-Hway Hseuh, J. Mater. Sci. Letters, 7 (1988) 497
- 52) J. Kim, C. Baillie and Y. Mai, Scripta metall. mater., 25 (1991) 315
- 53) J. Kerans and T.A. Parthasarathy, J. Am. Ceram. Soc., 74 (1991) 1585
- 54) D.B. Marshall, J. Am. Ceram. Soc., 67 (1984) C-259
- 55) D.B. Marshall and W.C. Oliver, J. Am. Ceram. Soc., 70 (1987) 542
- 56) J.W. Laughner, N.J. Shaw, R.T. Bhatt and J.A. Dicarlo, presented at 10th Annual Conference on Composites and Advanced Ceramic Materials, American Ceramic Society, Coco Beach, FL, 1986

- 57) P.D. Warren, T.J. Mackin and A.G. Evans, Acta metall. mater., **40** (1992) 1243
- 58) H.L. Cox, Brit. J. Appl. Phys. 3 (1952) 72
- 59) J. Bowling and G.W. Groves, J. Mater. Sci., 14 (1979) 431
- 60) J.D. Outwater and M.C. Murphy, in <u>Proceeding of The 24th Annual</u>

 <u>Technical Conference of The Reinforced Plastics/Composites Division.</u>

 The Society of the Plastics Industry, Inc. Washington DC. 1969, p. 11-c
- 61) D.K. Shetty, J. Am. Ceram. Soc., 71 (1988) C-107
- 62) J.D. Bright, D.K. Shetty, C.W. Griffin and S.Y. Limaye, J. Am. Ceram. Soc., 72 (1989) 1891
- 63) J.D. Bright, S. Danchaivijit and D.K. Shetty, J. Am. Ceram. Soc., 74
 (1991) 115
- 64) T.P. Weihs and W.D. Nix, J. Am. Ceram. Soc., 74 (1991) 524
- 65) T.P. Weihs, O. Sbaizero, E.Y. Luh and W.D. Nix, J. Am. Ceram. Soc., 74 (1991) 535
- 66) C-H Hsueh, J.D. Bright and D.K. Shetty, J. Mater. Sci. Letters, 10 (1991) 135
- 67) R.J. Kerans and T.A. Parthasarathy, J. Am. Ceram. Soc., **74** (1991) 1585
- 68) D.B. Marshall, M.C. Shaw and W.L. Morris, Acta. metall.mater.,40 (1992) 443
- 69) D.B. Marshall, Acta. metall. mater. 40 (1992)427
- 70) W.C. Carter, E.P. Butler and E.R. Fuller, Scripta metall.mater. 25 (1991) 579
- 71) T.J. Mackin, P.D. Warren and A.G. Evans, Acta. metall. mater. **40** (1992) 1251

- 72) S. Small, R.P. Vozzola and L.P. Zawada, J. Am. Ceram. Soc. **72** (1989) 1175
- 73) D.B. Marchall and B.N. Cox, Mech. Mech, Mater., 7 (1988)127
- 74) M.D. Thouless, Acta. metall., 37 (1989) 2297
- 75) M. R'Mili, D. Rouby, G. Fantozzi and P. Lamicq, Comp. Sci. Tech., 37 (1990) 207
- 76) M. Bouquet, J.M. Birbis and J.M. Quenisset, Comp. Sci. Tech., 37 (1990) 223
- 77) W.F. Brown, Jr. and J.E. Slawley, <u>Plain Strain Crack Toughness Testing</u>
 of High Strength Metallic Materials ASTM STP 410 (American Society
 for Testing and Materials, 1966)
- 78) D.B. Marshall and A.G. Evans, J. Am. Ceram. Soc., 68 (1985) 225
- 79) M.F. Ashby, Acta metall. mater., 41 (1993) 1313
- 80) J.R. Rice, J. Appl. Mech., 35 (1968) 379
- 81) G.I. Barenblatt, Advances in Applied Mechanics, 7 Academic Press, 1962
- 82) J. Aveston, G.A. Cooper and A. Kelly, in <u>Conference Proceedings on The Properties of Fiber Composites</u>, National Physical Laboratory, Teddington, UK 1971 (IPC Science and Technology Press, Guildford, 1971) pp 15-24
- 83) D.B. Marshall, B.N. Cox and A.G. Evans, Acta. metall., 33 (1985) 2013
- 84) R.W. Davidge, Composites, 18 (1987) 92
- 85) B. Budiansky, J.W. Hutchinson and A.G. Evans, J. Mech. Phys. Solids, 34 (1986) 167
- 86) M. Sutcu and W.B. Hillig, Acta metall. 38 (1990) 2653
- 87) R.N. Singh, J. Am. Ceram. Soc., 73 (1990) 2930
- 88) H.R. Schwietert and P.S. Steif, J. Mech. Phys. Solids, 38 (1990) 325

- 89) G.W. Sherer and S.M. Rekhson, J. Am. Ceram. Soc., 65 (1982) 399
- 90) K.M. Prewo, J. Mater. Sci., 17 (1982) 3549
- 91) H. Mecking, in <u>Proceedings of the 5th International Conference on Strength of Metals and Alloys</u>, Aachen, August 1979, edited by P. Haasen, V. Gerold and G. Kostorz (Pergamon Press, 1979) 1573
- 92) J. Morton and G.W. Groves, J. Mater. Sci., 11 (1976) 617
- 93) R.W. Rice, Cer. Eng. Sci. Proc., 2 (1981) 661
- 94) R.L. Lehman and C.A. Doughan, Comp. Sci. Tech., 37 (1990) 149
- 95) D.J. Green, P.S. Nicholson and J.D. Embury, J. Mater. Sci., 14 (1979)1413
- 96) R.U. Vaidya and K.N. Subramanian, J. Mater. Sci., 25 (1990) 3291